SUPERALLOWED β-DECAY BRANCHING RATIO MEASUREMENT OF ^{26}Si

A Dissertation

by

MIGUEL BENCOMO

Submitted to the Office of Graduate and Professional Studies of
Texas A&M University
in partial fulfillment of the requirements for the degree of

DOCTOR OF PHILOSOPHY

Chair of Committee,	John C. Hardy
Committee Members,	Dan Melconian
	Sherry Yennello
	Che-Ming Ko
Head of Department,	Grigory Rogachev

December 2018

Major Subject: Physics

ABSTRACT

As part of the continued effort to test the unitarity of the Cabbibo-Kobayashi-Maskawa matrix, the branching ratio for the $T_z = -1$ superallowed $0^+ \rightarrow 0^+$ positron-emitter ^{26}Si was measured precisely for the first time. Since the Q_{EC} value, 4840.86(10) keV, and half-life, 2245.3(7) ms, are known precisely, the branching ratio is all that is required to obtain a precise ft value. This completes the second pair of mirror superallowed transitions, ^{26}Si $\rightarrow$ ^{26m}Al and ^{26m}Al $\rightarrow$ ^{26}Mg. A previous measurement of the mirror transitions, ^{38}Ca $\rightarrow$ ^{38m}K and ^{38m}K $\rightarrow$ ^{38}Ar, showed that the ratio of mirror ft-values is very sensitive to the model used to calculate the small isospin symmetry-breaking corrections required to extract V_{ud}. In calculating this correction, both Woods-Saxon and Hartree-Fock radial wave functions have been used, with the experimental results from the first pair favoring Woods-Saxon. The result for the A = 26 mirror pair demonstrates that this conclusion can be generalized.

DEDICATION

To my parents

ACKNOWLEDGMENTS

First and foremost, I would like to thank my advisor, Dr. John C. Hardy, without whom this journey would not have been possible. His guidance, support and encouragement have been an inspiration. It has truly been a plasure working with him.

I would like to express my gratitude to Dr. Hyo-In Park, whose advice and insight have been of extreme importance to keep this project on track. Her dedication and work ethic are something I aspire to emulate.

Special thanks to Dr. Victor E. Iacob, for sharing his expertise and time with me. Our discussion involving detectors, electronics and coding have been a tremendous learning experience. I would like to thank all members of my research group, Dr. Ninel Nica, Dr. Vladimir Horvat and Dr. Lixin Chen who have always been there, to lend a hand and give advice, professionally and personally. The passion, determination, and knowledge of all members have been inspiring in the persuit of my degree.

I would like to extend my appreciation to the faculty and staff of the Cyclotron Institute at Texas A&M University. It has been an incredible experience watching, learning, and working side by side with all of you. You all create a great research environment and an enjoyable place to work. Special thanks to Dr. Brian Roeder and Dr. Antti Saastamoinen for providing the high-purity radioactive beams.

There are no words that can express the gratitude I have for my family. They have supported my endevours my whole life. Thank you for your love, support, encouragement and patience.

CONTRIBUTORS AND FUNDING SOURCES

Contributors

This work was supported by a dissertation committee consisting of Dr. John C. Hardy (advisor), Dr. Dan Melconian and Dr. Che-Ming Ko of the Department of Physics and Astronomy and Dr. Sherry Yennello of the Department of Chemistry.

The ROOT data sorting program used for this work was developed by Dr. Hyo-In Park and all EGSnrc Monte Carlo simulations were done by Dr. Victor E. Iacob.

All other work conducted for the dissertation was completed by the student independently.

Funding Sources

This work was supported by the U.S. Department of Energy under Grant No. DE-FG03-93ER40773 and by the Welch Foundation under Grant No. A-1397.

TABLE OF CONTENTS

Page

LIST OF FIGURES

FIGURE Page

LIST OF TABLES

1. INTRODUCTION

Superallowed $0^+ \rightarrow 0^+$ nuclear β decays provide, to date, the most demanding test of the unitarity of the Cabibbo-Kobayashi-Maskawa (CKM) matrix. The unitarity of this matrix is required in the description of electroweak interactions in the Standard Model. The most precise result comes from the top-row sum $|V_{ud}|^2 + |V_{us}|^2 + |V_{ub}|^2 = 0.99978 \pm 0.00055$ [1], where V_{ud} is by far the dominant term of the sum and also contributes equally with V_{us} to the uncertainty. While this result agrees with great precision with unitarity, efforts are still underway to decrease the uncertainty. Lowering the uncertainty will place tighter constraints on any new physics beyond the scope of the Standard Model.

In order to obtain V_{ud} it is necessary to determine the ft values for many superallowed transitions [2]. In order to determine these ft values, it is necessary to measure three quantities with very high precision: the total transition energy, Q_{EC}, the half-life, $t_{1/2}$, of the parent state, and the branching ratio, R, for the particular transition of interest. Once the ft values have been acquired, small theoretical corrections must be made. These corrections include radiative and isospin-symmetry-breaking effects [1, 3] which, when applied to the experimental data, give a consistent set of corrected $\mathcal{F}t$ values in agreement with the conserved vector current (CVC) hypothesis.

Some of these corrections depend on nuclear structure and have relatively large uncertainties as a result. However, these uncertainties can, in principle, be reduced by experiment. The comparison of ft values for mirror superallowed transitions, like ^{26}Si $\rightarrow$ ^{26m}Al and ^{26m}Al $\rightarrow$ ^{26}Mg, sensitively tests the isospin-symmetry-breaking corrections required to extract V_{ud} [4]. In determining the isospin-symmetry-breaking correction both Woods-Saxon (WS) and Hartree-Fock (HF) radial wave functions have been used. Without data on mirror decays there was not enough evidence to favor one over the other, giving a systematic uncertainty. The measurement of superallowed mirror transitions provides us with an opportunity to discriminate between the two potentials, possibly allowing a reduction of the uncertainty.

A set of mirror superallowed transitions, ^{38}Ca $\rightarrow$ ^{38m}K and ^{38m}K $\rightarrow$ ^{38}Ar, has already been measured, with results favoring the Woods-Saxon potential [4]. Determination of the *ft* value of ^{26}Si completes a second pair of mirror transitions, ^{26}Si $\rightarrow$ ^{26m}Al and ^{26m}Al $\rightarrow$ ^{26}Mg. The half-life [5], Q_{EC} value [6] and branching ratio [7] of ^{26}Si have already been measured but the precision of the previous branching-ratio measurement was not to the level required for the ft value comparison to be of significance.

2. BACKGROUND AND MOTIVATION

In this chapter all the relevant theories and previous measurements which this project has built upon will be presented. The information in this section ranges from Fermi's first theory of nuclear β decay to the most recent experiments in the field, as well as the results and conclusions gathered from said experiments.

2.1 The Standard Model and the weak interaction

The Standard Model of Particles is a theory that describes the strong, weak and electromagnetic particle interactions. According to this model two types of elementary particles exist: quarks and leptons, which are spin 1/2, also called Fermions. These quarks and leptons are classified into three generations, where each generation includes two quarks and two leptons. A classification of the three generations of particles is included in Table 2.1. For all these particles there exists an antiparticle with the same mass but opposite charge. As far as we know, all ordinary matter consists of first generation particles (*u, d, e,* ν_e): *i.e.*, the proton consists of *uud* while the neutron consists of *udd*.

All these particles experience the weak interaction, called this way since it is at least 10^{10} times weaker than the strong or the electromagnetic interactions. These weak interactions can change the flavors of quarks: for instance, an up-quark to a down-quark and vice versa, which account for nuclear β decay. In analogy to the radiative process of photon emission, via the electromagnetic interaction, which is described by the Lagrangian density,

$$\mathcal{L} = eJ_{\mu}^{(em)}A^{\mu} = e(\overline{\psi_p}\gamma_{\mu}\psi_p)A^{\mu}, \tag{2.1}$$

Fermi described beta decay in terms of hadronic currents, $J_{\mu}^{(n\to p)} = \overline{\psi_p}\gamma_{\mu}\psi_n$, leptonic currents, $J^{\mu}_{(\nu\to e)} = \overline{\psi_e}\gamma^{\mu}\psi_{\nu}$, and the Fermi coupling constant, G_V. The latter represents the strength of the weak interaction, and is analogous to e, the strength of the electromagnetic interaction.

Hence,

$$\mathcal{L}_\beta = G_V J_\mu^{(n\to p)} J^\mu_{(\nu\to e)} = G_V(\overline{\psi_p}\gamma_\mu\psi_n)(\overline{\psi_e}\gamma^\mu\psi_\nu), \tag{2.2}$$

where ψ_p, ψ_n, ψ_e, ψ_ν, are the wave functions for the proton, neutron, electron, and neutrino respectively. These interactions were first theorized by Fermi in 1933 [8] and expanded upon by Lee, Yang, Feynman and Gell-Mann later on. In addition to the particles described before, we have force-mediating particles with spin 1, known as bosons. The electromagnetic force is mediated by photon, the strong force by the gluon, while the weak interaction is mediated by three massive gauge bosons, the charged $W^\pm$ ($m_W = 80.399(23)\ GeV/c^2$) and the neutral Z^0 ($m_Z = 91.1876(21)\ GeV/c^2$), two of the heaviest particles yet detected.

	Quarks			Leptons		
Generation	Name	Symbol	Q/|e|	Name	Symbol	Q/|e|
First	up	u	$+2/3$	electron	e	-1
	down	d	$-1/3$	e-neutrino	ν_e	0
Second	charm	c	$+2/3$	muon	μ	-1
	strange	s	$-1/3$	μ-neutrino	ν_μ	0
Third	top	t	$+2/3$	tau	τ	-1
	bottom	b	$-1/3$	τ-neutrino	ν_τ	0

Gauge Bosons					
Name	Symbol	Q/|e|	Name	Symbol	Q/|e|
photon	γ	0	gluon	g	0
Z-boson	Z^0	0	W-boson	$W^\pm$	±1

Table 2.1: Standard model particles with quark and lepton classification as well as force mediating particles.

2.2 Cabbibo-Kobayashi-Maskawa matrix

The Cabbibo-Kobayashi-Maskawa (CKM) quark-mixing matrix is a central pillar of the Electroweak Standard Model. This 3x3 unitary rotation matrix relates the weak interaction

quark eigenstates to their mass eigenstates [9, 10]. By convention the CKM matrix is defined as

$$\begin{bmatrix} d' \\ s' \\ b' \end{bmatrix} = \begin{bmatrix} V_{ud} & V_{us} & V_{ub} \\ V_{cd} & V_{cs} & V_{cb} \\ V_{td} & V_{ts} & V_{tb} \end{bmatrix} \begin{bmatrix} d \\ s \\ b \end{bmatrix}, \tag{2.3}$$

where d, s, and b represent the mass eigenstates of the down, strange, and bottom quarks, while d', s', and b' represent their corresponding weak interaction eigenstates. All the mixing is expressed in term of the charge $-1/3$ quarks, while the charge $+2/3$ ones remain unmixed. The matrix elements represent the coupling of specified quark pairs. The Standard Model does not prescribe these matrix elements but it does require the matrix to be unitary. Thus the elements must be determined experimentally and the unitarity tested via the orthonormality of rows and columns or the normalization of rows and columns. To date the most precise test of unitarity comes from the top row sum where the up quark mixes with the down, strange and bottom quarks, $|V_{ud}|^2 + |V_{us}|^2 + |V_{ub}|^2$. The term V_{ud} is by far the dominant term. This term can be obtained from different sources such as nuclear superallowed β decays, the β-decay of odd-mass mirror nuclei, neutron β decay, and pion β decay. The V_{us} term is determined from K-meson decays. The last term, V_{ub} is determined from B-meson decays, but is too small to impact the unitarity test at the current level of precision on the first two terms.

2.3 Nuclear β decay

Nuclear β decay is a weak-interaction process whereby one of the protons or neutrons inside a nucleus of mass number A = Z + N is transformed in order to achieve an energetically more stable configuration. During this process the total number of nucleons remains unchanged. In β^- decay a neutron is converted to a proton with the emission of an electron

and an anti-electron neutrino

$$ {}^{A}_{Z}\mathrm{X}_{N} \rightarrow {}_{Z+1}{}^{A}\mathrm{Y}_{N-1} + e^{-} + \overline{\nu_e}. \tag{2.4} $$

In β^+ decay, a proton is converted to a neutron with the emission of a positron and an electron neutrino,

$$ {}^{A}_{Z}\mathrm{X}_{N} \rightarrow {}_{Z-1}{}^{A}\mathrm{Y}_{N+1} + e^{+} + \nu_e. \tag{2.5} $$

A third weak-interaction process, is electron capture (EC) decay, whereby the nucleus captures an electron from one of the atomic orbitals, changing a proton to a neutron and emitting an electron neutrino,

$$ e^{-} + {}^{A}_{Z}\mathrm{X}_{N} \rightarrow {}_{Z-1}{}^{A}\mathrm{Y}_{N+1} + \nu_e. \tag{2.6} $$

When an isotope decays, the energy released in the process is known as the Q value. This can be expressed in terms of the difference between parent and daughter nuclei:

$$ Q_{\beta^-} = [m({}^{A}_{Z}\mathrm{X}_{N}) - m({}_{Z+1}{}^{A}\mathrm{Y}_{N-1})]c^2 \tag{2.7} $$

$$ Q_{\beta^+} = [m({}^{A}_{Z}\mathrm{X}_{N}) - m({}_{Z-1}{}^{A}\mathrm{Y}_{N+1})]c^2 - 2m_e c^2 \tag{2.8} $$

$$ Q_{ec} = [m({}^{A}_{Z}\mathrm{X}_{N}) - m({}_{Z-1}{}^{A}\mathrm{Y}_{N+1})]c^2, \tag{2.9} $$

where m_e represents the mass of the electron, $m({}^{A}_{Z}\mathrm{X}_{N})$ the mass of the parent nucleus and $m({}_{Z\pm1}{}^{A}\mathrm{Y}_{N\mp1})$ the mass of the daughter nucleus. Although β^+ decay and ec decays are competing processes yielding the same daughter nucleus, the Q-values for these reactions are different. Taking the difference between the two results in an energy difference of $2m_e c^2$ (1022 keV). The β^+ decay process is therefore only possible when the rest-mass energy difference between the parent and daughter states is greater than 1022 keV; otherwise the transition decays by electron capture exclusively.

The energy released in these decay processes can be converted to the kinetic energy of the

decay products, or it can excite the daughter atom and/or nucleus. Considering conservation of energy for the 3-body final state of $\beta^{\mp}$ decays we obtain

$$Q_{\beta} = T_{\beta} + T_{\nu_e} + T_D + E_D^* + E_{D_e}^*, \tag{2.10}$$

where T_{β}, T_{ν_e} and T_D represent the kinetic energy of the β particle, neutrino and daughter nucleus, respectively, E_D^* represents the excitation energy of the daughter nucleus, and $E_{D_e}^*$ represents the excitation energy of the daughter atom. The daughter nucleus will recoil following the decay to conserve momentum, but since it is much heavier than either the β particle or neutrino, it generally does so with very little kinetic energy. The conservation of momentum and energy equations are then generally, to first order, well approximated by:

$$\vec{p}_{\beta} + \vec{p}_{\nu_e} + \vec{p}_D = 0. \tag{2.11}$$

$$T_{\beta} + T_{\nu_e} \approx Q_{\beta\pm}, \tag{2.12}$$

These equations provide a continuum of solutions for the kinetic energies of the β particle and neutrino, where the maximum kinetic energy of the β particle (T_{β}^{max}) occurs when the neutrino is emitted with zero kinetic energy, and the maximum kinetic energy of the neutrino ($T_{\nu_e}^{max}$) occurs when the opposite happens. The β decay Q-value can be then determined by measuring the β energy distribution to determine the endpoint energy. With the current level of precision, recoil-order corrections need to be taken into account. These corrections are kinematic corrections which, in the most precise work, cannot generally be ignored. This correction is applied later to the statistical rate function $f(Z, Q_{EC})$ (explained in Section 5), which slightly modifies the end-point energy and additionally affects the shape-correction function in f.

2.3.1 Selection rules and superallowed β decays

All β decays can be classified into allowed and forbidden transitions. In the allowed approximation, the electron and neutrino are created at a point; therefore they do not carry any angular momentum, $L = 0$, and the only change in the angular momentum of the nucleus must result from the spins of the the electron and neutrino, each of which has a value of $S = 1/2$. These two lepton spins can couple antiparallel (total $S = 0$), also known as Fermi transitions, or parallel (total $S = 1$), also called Gamow-Teller transitions. This means that the total angular momentum, J, is changed by 0 or 1. If the electron and neutrino carry no orbital angular momentum, then the parities of the initial and final states remains the same. When L $>$ 0 , the transition is referred to as forbidden, with the value of L giving the level of forbiddeness. These decays are not strictly forbidden but are less probable and may involve a change of parity. This change is based on parity selections rules $\Delta\pi = (-1)^L$, with $\Delta\pi = 1$ or -1 correspond to no parity or parity change respectively. Since the proton and the neutron have nearly identical masses, and behave nearly identically under the strong force, the concept of isospin is used in the description of nucleons. Isospin in nuclear physics treats protons and neutrons bound in a nucleus as two different states of one single particle, the nucleon. For a nucleon with an isospin of $T = 1/2$, the proton state is represented by the down projection to the quantized axis, $T_z = -1/2$, and the neutron state is represented by the up projection $T_z = +1/2$. The total isospin z-projection of the nucleus, T_z, is the sum of isospin z-projections of all nucleons, defined as [11],

$$T_z = \frac{N - Z}{2}. \tag{2.13}$$

The total isospin of the nucleus, T, can then take any integer value in the range

$$\frac{|N - Z|}{2} \leq T \leq \frac{N + Z}{2}. \tag{2.14}$$

For almost all nuclei, the ground state has the lowest possible total isospin of $T = |T_z|$. The only exceptions come from odd-odd N = Z nuclei, many of which have ground state isospin T = 1. Fermi transitions are restricted to those with $\Delta T = 0$ transitions and Gamow-Teller transitions to $\Delta T = 0, \pm 1$. The selection rules for allowed transitions are summarized in Table 2.2.

Fermi transitions	
$J_f = J_i$	$(\Delta J = 0)$
$T_f = T_i$	$(\Delta T = 0)$
$T_{zf} = T_{zi} \mp 1$	$(\Delta T_z = \pm 1)$
$\Delta\pi = 0$	no parity change
Gamow-Teller transitions	
$\Delta J = 0, 1$	$(J_i = 0 \rightarrow J_f = 0$ are forbidden)
$\Delta T = 0, \pm 1$	
$T_{zf} = T_{zi} \mp 1$	$(\Delta T_z = \pm 1)$
$\Delta\pi = 0$	no parity change

Table 2.2: Selection rules for allowed transitions

Superallowed Fermi β decays refer to the allowed, $L = 0$, pure Fermi, $S = 0$, transitions between 0^+ isobaric analogue states, $\Delta T = 0$, where the only difference between parent and daughter states is the change of a proton in the parent to a neutron in the daughter. Since they are $J_i = 0 \rightarrow J_f = 0$ and there is no parity change, these transitions are pure vector transitions nearly independent of nuclear structure.

2.3.1.1 Isobaric multiplet mass equation

Isospin is not an exact symmetry, the isotropy of isospin space is broken by the electromagnetic interaction, neglecting the mass difference between u and d quarks. Charge-dependent couplings break the $(2T+1)$-fold degeneracy that leads to the existence of isospin multiplets. The members of a given multiplet are labelled by T_z taking values between $-T$ and T. The isobaric multiplet mass equation (IMME) first proposed by Wigner in 1957 [12]

uses a simple model to describe isospin multiplets where the level schemes of each nucleus would be shifted by the Coulomb energy and the neutron-proton mass difference. Since the charge-independent Hamiltonian, H_{CI}, conserves T, its eigenvalues are independent of T_z but depend on other quantum numbers labeled α:

$$H_{CI}|\alpha T T_z\rangle = E_{\alpha,T}|T T_z\rangle. \tag{2.15}$$

A charge-dependent two-body force can be expressed in terms of isospin by,

$$V_{ij} = V_1(t_{zi} + t_{zj}) + V_2(t_{zi}t_{zj}), \tag{2.16}$$

where, i and j label the particles and t_{zi} and t_{zj} their isobaric spin projection. V_{ij} can be written as a linear combination of scalar, vector, and tensor terms. Therefore, the perturbing Hamiltonian, H', can be written as:

$$H' = H^{(0)} + H^{(1)} + H^{(2)}, \tag{2.17}$$

with $H^{(n)}$ being the nth order isotensor with zero projection on the z axis. Applying the Wigner-Eckart theorem [13] to states which are eigenvalues of H_{CI} yields matrix elements expressed as products of reduced matrix coefficients and Clebsch-Gordan coefficients,

$$\begin{aligned} \langle \alpha T T_z|H'|\alpha T T_z\rangle &= \langle \alpha T||H^{(0)}||\alpha T\rangle \\ &+ \frac{T_z}{[T(T+1)]^{1/2}}\langle \alpha T||H^{(1)}||\alpha T\rangle \\ + \frac{3T_z^2 - T(T+1)}{[(2T-1)T(T+1)(2T+3)]^{1/2}}&\langle \alpha T||H^{(2)}||\alpha T\rangle. \end{aligned} \tag{2.18}$$

All terms of the expression above are energies expressed in terms of the reduced matrix element and coefficients involving T and T_z. Therefore, the relation between masses of a

given multiplet can be written to first order as:

$$\langle \alpha T T_z | H_{CI} + H' | \alpha T T_z \rangle = M(T_z) = a + bT_z + cT_z^2. \tag{2.19}$$

The coefficients of the IMME are later used in the calculations of the isospin-symmetry-breaking correction.

2.4 Conserved vector current hypothesis

All of the particles involved in the β-decay process are spin-1/2 fermions. The β and neutrino can be emitted with their intrinsic spin angular momentum coupled to S = 0 or 1. The Fermi and Gamow-Teller couplings have different intrinsic strengths, as well as different operators, and so the matrix element must be separated as

$$g^2|M|^2 = G_V^2|M_F|^2 + G_A^2|M_{GT}|^2, \tag{2.20}$$

where G_V is the weak-interaction vector coupling constant, and G_A is the axial-vector coupling constant. While the description of β decay in the minimal electroweak model involves both vector and axial-vector interactions, the absence of any angular momentum transfer in $0^+ \rightarrow 0^+$ transitions implies that these decays, neglecting radiative corrections for the moment, are governed entirely by the vector component $g^2|M|^2 = G_V^2|M_F|^2$ and contain contributions from the axial-vector coupling only through small higher-order radiative corrections.

The conserved vector current (CVC) hypothesis, put forward in 1958 by Feynman and Gell-Mann [14], asserts that the value of G_V is unmodified in the presence of the strong nuclear force, and its value should therefore be constant and independent of the particular nucleus in which it is measured. The fact that the value of G_V extracted from the superallowed data is currently found to be constant across 14 precisely measured decays spanning atomic numbers from Z = 6 to Z = 37 is a strong vindication of the CVC hypothesis. In

addition to providing the most demanding test of the CVC hypothesis, superallowed decays also provide stringent limits on many possible extensions to the standard electroweak model.

2.4.1 The ft values

The measured strength of a β transition is known as the ft-value. Experimentally, the ft value is determined from three measured quantities: the total transition energy, Q_{EC}, the half-life, $t_{1/2}$, of the parent state, and the branching ratio, R, for the particular transition of interest. The Q_{EC}-value is required to determine the phase-space integral, f, while the half-life and branching ratio combine to yield the partial half-life, t. For superallowed $0^+ \rightarrow 0^+$ decays the ft value is directly related to the vector coupling constant, G_V. So, according to the CVC hypothesis discussed in Section 2.4, the measured ft values should be the same for all superallowed $0^+ \rightarrow 0^+$ transitions regardless of the nuclei. The ft value for superallowed decays is written as,

$$ft = \frac{K}{G_V^2 \langle M_F \rangle^2}, \tag{2.21}$$

where $K/(\hbar c)^6 = 2\pi\hbar \ln 2/(m_e c^2)^5 = 8120.2787(11) \times 10^{10}\ GeV^{-4}s$ and $\langle M_F \rangle$ the Fermi matrix element is given by,

$$\begin{aligned} \langle M_F \rangle^2 &= \langle JMT_f T_{zf} | \tau_\pm | JMT_i T_{zi} \rangle^2 \\ &= T_i(T_i + 1) - T_{zi} T_{zf}, \end{aligned} \tag{2.22}$$

where i and f represent the initial and final states, and $\tau_\pm$ is the isospin ladder operator

$$\tau_\pm |T, T_z\rangle = \sqrt{(T \mp T_z)(T \pm T_z + 1)} |T, T_z \pm 1\rangle, \tag{2.23}$$

connecting members of an isospin multiplet with the same total isospin but different isobaric analogue states. For the case of superallowed transitions within a $J^\pi = 0^+$ and $T = 1$ isospin multiplet, the Fermi matrix element value becomes $\langle M_F \rangle^2 = 1(1+1) = 2$ since either T_{zi} or

T_{zf} are zero. From Eq. 2.21, we can see that the ft values for superallowed $0^+ \rightarrow 0^+$ β decays are the same regardless of the nuclei involved, given that G_V is a constant as described by the CVC hypothesis. In practice, the expression for the ft value must incorporate several small correction terms, which account for radiative and isospin symmetry-breaking effects: *i.e.* isospin is not an exact symmetry in nuclei due to the Coulomb interaction between protons and charge dependence in the nuclear force. These corrections will be discussed further in the next section; for now it is worth noting that these corrections can be combined with the ft values to define a "corrected" $\mathcal{F}t$ value denoted by [3],

$$\mathcal{F}t = ft(1+\delta'_R)(1+\delta_{NS}-\delta_C) = \frac{K}{2G_V^2(1+\Delta_R^V)}, \tag{2.24}$$

where δ'_R, δ_{NS}, Δ_R^V are radiative corrections and δ_C is a correction for isospins-symmetry breaking. The corrections modify the ft values by at most a few percent. Generally the calculations have been made with an accuracy of 10% of their central value, so the theoretical precision in Eq. 2.24 contributes $\pm 0.1\%$. This has motivated experiment to reach the same level or better.

2.4.1.1 Radiative corrections

In a beta-decay half-life experiment, the rate measured includes not only the bare decay but also radiative decay processes such as the emission of bremsstrahlung and the exchange of virtual photons and Z-bosons. Conventionally, the radiative correction has been separated into two parts, one that contains the nucleus-dependent terms, called the "outer" radiative correction, δ_R and one that is independent of the nucleus, the "inner" radiative correction, Δ_R^V. The best value for the nucleus-independent correction to date comes from the work of Marciano and Sirlin [15, 16],

$$\Delta_R^V = 2.361 \pm 0.038\%. \tag{2.25}$$

The nucleus dependent correction is separated into two parts,

$$\delta_R = \delta'_R + \delta_{NS}. \tag{2.26}$$

The nuclear-structure independent term, δ'_R, depends only on the charge of the daughter nucleus, Z, as well as the end-point energy, W_0, of the transition. The nuclear-structure dependent term, δ_{NS}, is a second-order correction arising from a weak axial-vector interaction. While superallowed $0^+ \rightarrow 0^+$ transitions are purely vector, in second order a weak axial-vector interaction can combine with an electromagnetic interaction to produce a perceptible contribution. The first interaction flips a nucleon spin and then a virtual photon emitted by the departing positron flips it back, making the whole process look like a pure vector interaction from the intrinsic spin point of view. Two interactions can occur on the same nucleon or on two separate ones. The computation for the latter depends on nuclear structure, the result being δ_{NS}. A shell model calculation is used to obtain δ_{NS} [17, 3]. Recently, a new calculation for Δ_R^V has appeared in the arXiv with a lower value and better precision [18]. Since the new value has not been published or confirmed it will not be considered further.

2.4.1.2 Isospin symmetry-breaking corrections

As isospin is not an exact symmetry in nuclei because of the Coulomb force, as well as charge-dependent nuclear forces, the Fermi matrix element is quenched according to

$$|M_F|^2 = |M_F^0|^2(1 - \delta_C), \tag{2.27}$$

where M_F^0 is the exact symmetry value, $|M_F^0| = \sqrt{2}$, and δ_C is the isospin-symmetry-breaking correction. This correction can be, to first order, divided into two independent parts

$$\delta_C = \delta_{C1} + \delta_{C2} \tag{2.28}$$

The first term, δ_{C1}, accounts for different amounts of configuration mixing in the parent 0^+ state and the 0^+ isobaric analogue state in the daughter nucleus caused by Coulomb and isospin non-conserving components of the residual interaction acting within the shell-model calculation model space. For δ_{C1}, a modest shell-model space is employed, in which Coulomb and other charge-dependent terms are added to the charge-independent effective Hamiltonian customarily used for the shell model. These charge-dependent additional terms are separately adjusted for each superallowed β transition to reproduce the b and c coefficients of the isobaric multiplet mass equation (IMME, Eq. 2.19) for the triplet of $T = 1$, 0^+ states that includes the parent and daughter states of the transition. The latter is achieved by adjusting the strength of the Coulomb interaction among the valence protons so that the measured b coefficient in the IMME is exactly reproduced, while the charge-dependent nuclear interaction in the shell-model Hamiltonian is tuned to reproduce the measured c coefficient of the IMME. The parameters used for the shell-model calculations were taken from the literature, based on on a wide range of independent spectroscopic data for nearby nuclei. The value for this term is given by the average of these results and the uncertainty reflects the spread of said results.

The second term, δ_{C2}, accounts for the imperfect overlap of the proton and neutron radial wave functions due to differences in binding energy and the Coulomb potential experienced by the proton. Since the Coulomb force is long range, its influence in configuration space extends much further than the single major oscillator shell included in the calculation of δ_{C1}. This results in proton radial functions that differ from the neutron ones so, when the overlap is computed, its departure from unity determines the value of δ_{C2}. The nucleon radial wave functions required for the δ_{C2} calculation are taken to be eigenstates of a Woods-Saxon (WS) and Coulomb potential, adjusted to reproduce the proton and neutron separation energies, and with full parentage expressions from the shell-model calculations. The radius parameter of this potential is determined by requiring that the charge density constructed from the proton eigenfunctions yields a root-mean-charge radius in agreement with the experimental

value. Similarly, δ_{C2} can be calculated using eigenfunctions of a self-consistent Hartree-Fock (HF) mean-field potential rather than the phenomenological Woods-Saxon potential. The initial and final states of the β transition consisted of a core of (A - 1) nucleons, to which the last proton or neutron is bound, and spherical Skyrme-Hartree-Fock calculations for the core are used to obtain the mean fields. In particular, the asymptotic form of the proton radial wave function in the parent nucleus is taken as a proton bound to a core of charge Z rather than the Z + 1 charge of the parent nucleus. The two sets of calculations exhibit the same behavior. However, the HF calculations are consistently lower than the WS, creating a systematic uncertainty since, until recently, we have not been able to discard either method with confidence.

The uncorrected ft values for the 14 most precisely measured transitions scatter over a range of 2%; however after combining the aforementioned corrections, the corrected $\mathcal{F}t$ values must be consistent with one another if the CVC hypothesis is to be satisfied. This requirement also serves as a sensitive test of the reliability of the calculations used for the structure dependent terms δ_C and δ_{NS}.

2.5 Current status of world data

The latest critical survey of world data for superallowed $0^+ \rightarrow 0^+$ beta decays was published in 2015 [1]. This survey includes 222 individual measurements of comparable precision for Q_{EC}, $t_{1/2}$, and R. The world average ft values are obtained from 18 complete sets of superallowed transitions as well as corrected $\mathcal{F}t$ values, fourteen of which have a precision of order 0.1% or better (^{10}C, ^{14}O, ^{22}Mg, ^{26m}Al, ^{34}Cl, ^{34}Ar, ^{38m}K, ^{38}Ca, ^{42}Sc, ^{46}V, ^{50}Mn, ^{54}Co, ^{62}Ga, ^{74}Rb) leading to a very precise determination of the consistency of CVC and the value of V_{ud}. The new average value of $\mathcal{F}t$ obtained from the survey was $\overline{\mathcal{F}t} = 3072.27 \pm 0.72$ s. From this we can determine the new value of V_{ud}, which is derived

from the vector coupling constant, G_V and the weak interaction coupling constant, G_F,

$$V_{ud} = \frac{G_V}{G_F}, \tag{2.29}$$

where G_F is determined from the purely leptonic muon decay and its value, as determined by the Particle Data Group (PDG), is $G_F/(\hbar c)^3 = 1.1663787(6) \times 10^{-5}\ GeV^{-2}$ [19]. Since $\overline{\mathcal{F}t}$ is inversely proportional to G_V^2 we can rewrite Eq. 2.29 as

$$V_{ud}^2 = \frac{K}{2G_F^2(1+\Delta_R^V)\overline{\mathcal{F}t}}. \tag{2.30}$$

The value of V_{ud} from superallowed $0^+ \rightarrow 0^+$ beta decays is then,

$$|V_{ud}| = 0.97417 \pm 0.00021[1]. \tag{2.31}$$

As mentioned in section 2.2, this term can be obtained from different sources. Neutron β decay provides an important advantage in the analysis since it does not require the application of corrections for isospin-symmetry breaking or for nuclear structure-dependent radiative effects. It also has some disadvantages; neutrons are hard to confine and their decay is not restricted to vector weak interaction. The axial-vector current is also present, so in addition to the ft-value some other measurements are required to determine the ratio of the vector to axial-vector contributions. The nuclear $T = 1/2$ mirror decays, also require an additional correlation measurement to determine the weak vector contribution from the axial-vector one and do not provide any simplification to the nuclear structure-dependent corrections. Pion β decay in principle should be the best way to determine V_{ud}. Like superallowed decays, it is a pure vector decay between spin-0 states of an isospin triplet without the uncertainties of nuclear structure effects. Unfortunately, the branching ratio is very small, of the order of 10^{-8}, and difficult to measure with sufficient precision. To date, the most precise value for V_{ud} comes from the measurement of superallowed β^+ emitters, which when

combined with the best known values of V_{us} and V_{ub} provides the most precise test for the unitarity of the CKM matrix. The top row sum then provides the following result:

$$|V_{ud}|^2 + |V_{us}|^2 + |V_{ub}|^2 = 0.99978 \pm 0.00055[1]. \tag{2.32}$$

This result confirms unitarity.

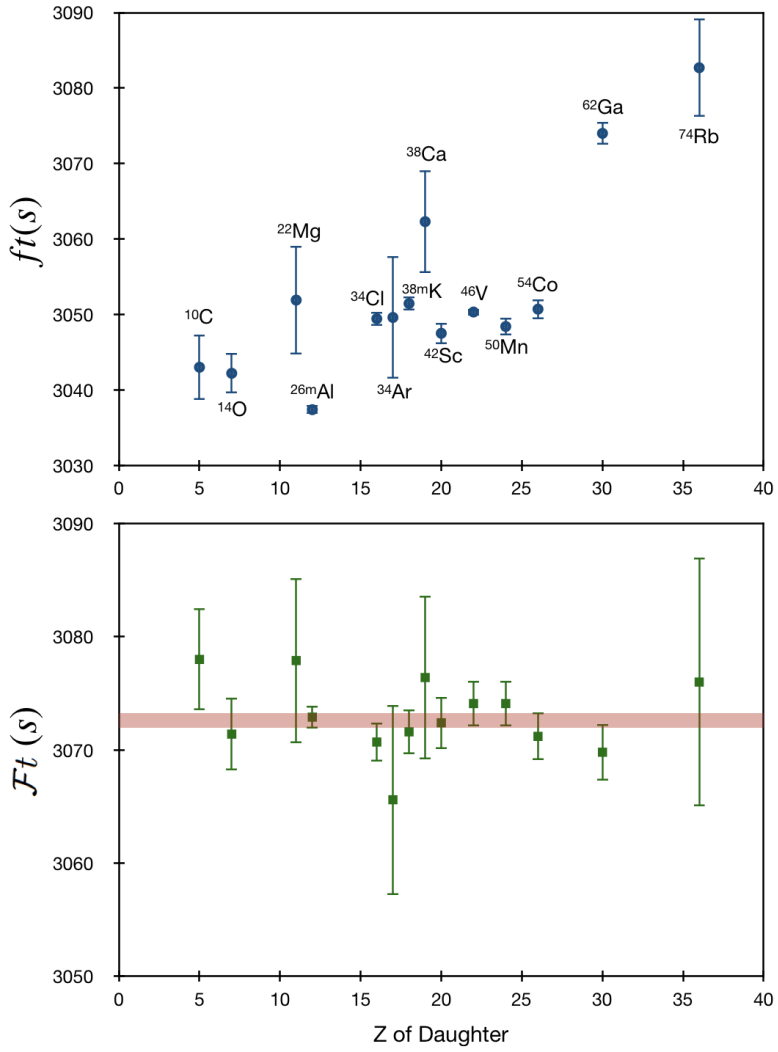

Figure 2.1: The top plot shows the uncorrected experimental ft values as a function of the charge on the daughter nucleus. The bottom plot shows the corresponding $\mathcal{F}t$ values; they differ from the ft values by the inclusion of the correction terms δ'_R, δ_{NS}, and δ_C. The horizontal red band gives one standard deviation around the average $\mathcal{F}t$ value (Adapted from [1]).

2.5.1 Mirror superallowed pairs

With the 2014 addition of ^{38}Ca [4, 20] to the 13 well known transitions, an opportunity has been created for the first time to make a high-precision comparison of the ft values from a pair of mirror superallowed decays, ^{38}Ca $\rightarrow$ ^{38m}K and ^{38m}K $\rightarrow$ ^{38}Ar. The ratio of mirror

ft values is very sensitive to the model used to calculate the isospin-symmetry-breaking correction, δ_C. Since the uncertainty in these corrections contributes significantly to the uncertainty both on V_{ud} and on the unitarity sum, experimental constraints imposed by mirror ft-value ratios can serve to reduce those uncertainties by up to 10%. Accepting the constancy of $\mathcal{F}t$ values, we can use Eq. 2.24 to write the ratio of experimental ft values for a pair of mirror superallowed transitions as follows,

$$\frac{ft^a}{ft^b} = 1 + (\delta_R^{'b} - \delta_R^{'a}) + (\delta_{NS}^b - \delta_{NS}^a) - (\delta_C^b - \delta_C^a) \tag{2.33}$$

where superscript "a" denotes the decay of the $T_Z = -1$ parent and "b" the decay of the $T_Z = 0$ parent.

The advantage to using this ratio is that the uncertainty on a difference term such as $(\delta_C^b - \delta_C^a)$ is significantly less than the uncertainties on δ_C^b and δ_C^a individually. This arises from the way in which the uncertainties were determined (see Section 2.4.1.2). For example, the value of δ_C was determined to be the average of the results obtained from different parameters while the uncertainty represents the spread of those results. If the same method is used for the mirror term $(\delta_C^b - \delta_C^a)$, the spread from those results is less than that of δ_C^b and δ_C^a individually.

Furthermore, the isospin correction term δ_{C2} discussed earlier is a source of theoretical uncertainty that arises from the choice of potential used to obtain the parent and daughter radial wave functions. Both Woods-Saxon (WS) and Hartree-Fock (HF) eigenfunctions have been used but there is a consistent difference between their results. Consequently a "systematic" uncertainty corresponding to half the difference has in the past been assigned to δ_{C2}. With the statistical uncertainty contribution from δ_C reduced in the mirror ft-value ratio, Eq. 2.33 offers the opportunity to use experiment to distinguish cleanly between WS and HF radial wave functions. If one set of calculations were to be convincingly eliminated, then the systematic uncertainty on δ_C could also be eliminated and the uncertainty in V_{ud}

reduced. Table 2.3 shows the calculated mirror ft-value ratios using WS and HF radial wave functions for the four cases of interest. These values were taken from the most recent survey [1].

	ft^a/ft^b	
Mirror pairs	WS	HF
^{26}Si $\rightarrow$ ^{26m}Al; ^{26m}Al $\rightarrow$ ^{26}Mg	1.00389(26)	1.00189(26)
^{34}Ar $\rightarrow$ ^{34}Cl; ^{34}Cl $\rightarrow$ ^{34}S	1.00171(26)	0.99971(43)
^{38}Ca $\rightarrow$ ^{38m}K; ^{38m}K $\rightarrow$ ^{38}Ar	1.00196(39)	0.99976(43)
^{42}Ti $\rightarrow$ ^{42}Sc; ^{42}Sc $\rightarrow$ ^{42}Ca	1.00566(65)	1.00296(42)

Table 2.3: Calculated ft^a/ft^b ratios for four doublets with WS and HF radial wave functions used to calculate δ_C. The uncertainties due to differences in δ'_R, δ_{NS}, and δ_C are all incorporated.

It can be seen in Figure 2.2 that the result from the $A = 38$ case favors the WS calculation, however it is not yet definitive. The current capabilities for producing superallowed $T_Z = -1$ parent nuclei provide an opportunity for high statistics measurements of at least other three mirror pairs, $A = 26, 34$, and 42. With the branching ratio measurement of ^{26}Si from this project, we will be able to determine a precise ft value for ^{26}Si, as well as the ratio of ft values for the A = 26 pair. Similar to the case of ^{26}Si, a new branching ratio measurement of ^{34}Ar leading to smaller uncertainties would provide a mirror ft-value for $A = 34$. For the case of $A = 42$, a half-life and branching ratio measurement of ^{42}Ti are still needed.

Although we are only using mirror ft value ratio to test the isospin-symmetry-breaking correction, δ_C, this principle can also be use to test the nuclear-structure dependent term, δ_{NS}, and the nuclear-structure independent term, δ'_R. However, the uncertainty in δ'_R is a smooth function of Z^2 [17] in which case this test would serve no real purpose.

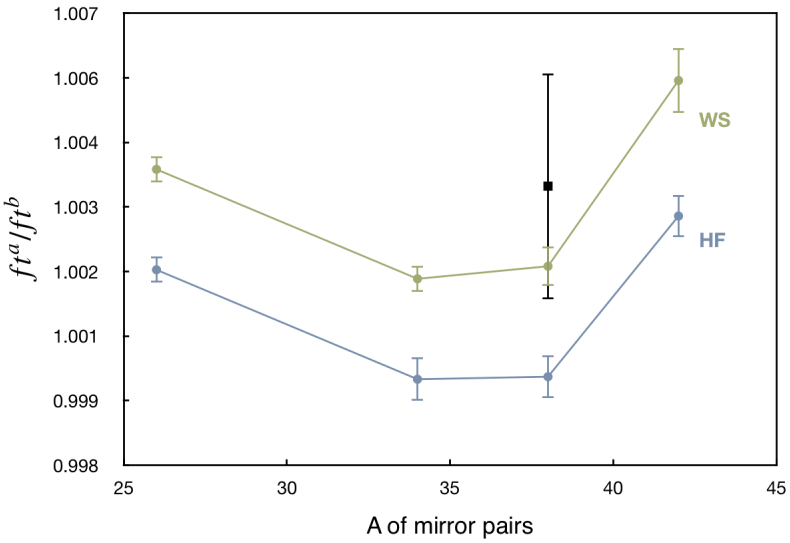

Figure 2.2: Calculated mirror-pair ft^a/ft^b values for $A = 26, 34, 38$, and 42, the four cases currently accessible to high-precision experiment. The green and blue lines connect calculated results that utilize Woods-Saxon (WS) and Hartree-Fock (HF) radial wave functions, respectively. The measured result for the A = 38 mirror pair is shown as the black square with error bars (Adapted from [4]).

3. EXPERIMENTAL OVERVIEW

For this experiment a pure beam of radioactive ^{26}Si was produced using Texas A&M's K500 superconducting cyclotron and the Momentum Achromat Recoil Spectrometer (MARS). This beam was implanted in the aluminized mylar tape of a fast tape-transport system. Collected samples were periodically moved to a shielded counting location where β-γ coincidences were measured, using a high-purity germanium detector (HPGe) as well as a plastic scintillator. A more detailed description of the equipment and the experimental setup is given in this chapter.

3.1 Momentum Achromat Recoil Spectrometer

The Momentum Achromat Recoil Spectrometer separates rare isotopes from background activities, allowing in our case the study of their β-decay properties. MARS is able to operate over a broad energy range with good mass resolution and high efficiency [21]. Stable beams from the Texas A&M University K500 superconducting cyclotron interact via inverse kinematic transfer reactions with a gas target at the MARS target chamber (schematic shown in Figure 3.1). For our measurement the gas cell is operated at LN_2 temperatures to increase the gas density. The entrance and exit windows of the cell use 4 μm thick Havar where degraders and stripper foils can be placed to tune the final beam energy and ensure fully-stripped ejectiles. The recoil spectrometer is used to filter reaction products into secondary beams. MARS has two dispersive planes. Particles that pass through the quadrupole doublet Q1-Q2 and the first dipole D1 have a maximum momentum dispersion near the entrance to the quadrupole singlet Q3 located at the middle of the spectrometer. The combination of the first three quadrupoles and first two dipoles produces an achromatic and nearly parallel beam into the velocity filter, a conventional $E \times B$ filter with a vertical electric field. The last dipole D3 bends the beam vertically to match the momentum dispersion to the velocity

dispersion and along with the quadrupole doublet Q4-Q5 produces an m/q mass focus at the MARS focal plane. Slits (Slit 1) are located at the entrance to MARS to control the solid-angle acceptance. Horizontal momentum selection slits (Slit 2h) are located just in front of Q3. A set of vertical slits, Slit 2v, are used to limit the vertical extent of the recoil ions as they enter D2 and the velocity filter. Two sets of slits are located after Q5. The slits labeled Slit 3 are used to define the solid angle of the secondary beam. Slits (Slit 4) are located just in front of the mass focal plane and are used to accept only a particular value of m/q. More information can be found in [21, 22].

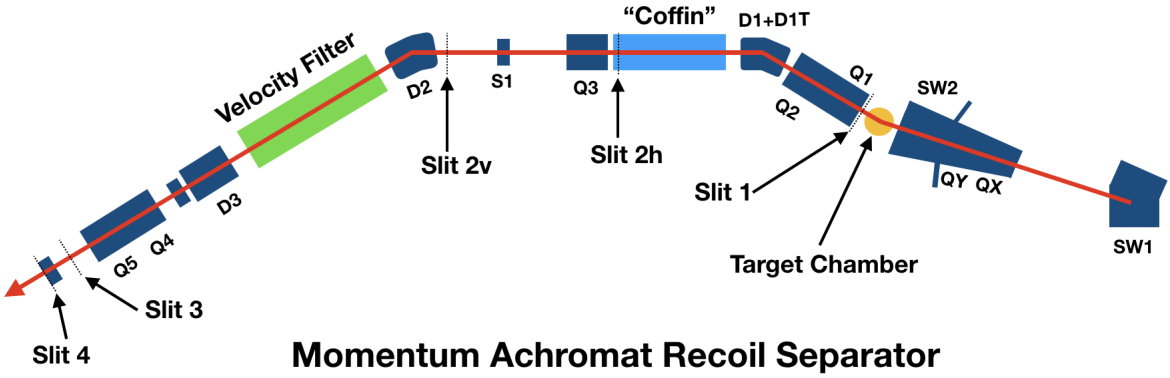

Figure 3.1: Schematic view of the recoil spectrometer MARS.

3.1.1 ^{26}Si production

We obtained ^{26}Si by using a production reaction with inverse kinematics, $p(^{27}\mathrm{Al},2n)^{26}\mathrm{Si}$, and selecting the desired reaction product with the Momentum Achromat Recoil Separator. Our primary beam of 30A MeV ^{27}Al impinged on a 2-atm hydrogen gas target cooled to liquid nitrogen temperature. The fully stripped ejectiles were then analyzed by MARS. Initially, working with a low-current primary beam, we inserted at the focal plane of MARS a 5 $\times$ 5 cm position-sensitive silicon detector (PSSD) consisting of 16 strips 300 μm thick, backed by a 1-mm-thick detector. The PSSD was used first for the identification of secondary reaction products, then for the control of the selection and focus of the desired species in the center of the beam line. Figure 3.2 shows the results obtained after the spectrometer had been tuned for ^{26}Si and slits (Slit 4 in Figure 3.1) set to $\pm$1.6 mm. This also gave us a clear indication of nearby reaction products that could potentially contribute as impurities to our selected beam. The principal surviving impurities for this experiment can be seen to be ^{24}Al, ^{22}Mg, ^{23}Mg, and ^{15}O.

After the tuning and selection procedure, the PSSD was removed from the beam path and the intensity of the primary beam increased. With extraction slits at the MARS focal plane used to select ^{26}Si, the resulting radioactive beam was extracted into air through a 50-μm-thick kapton window. This beam, passed through a 0.3-mm thin BC-404 plastic scintillator, where the ions were detected, and then through a set of aluminum degraders, eventually being implanted in the 76-μm-thick aluminized Mylar tape of a fast tape-transport system. The m/q selectivity in MARS led to a 98.7% pure beam of ^{26}Si. The purity of the beam is further increased for the measurement using the aforementioned Al degraders, this procedure will be explained in detail in Section 4.3.1.

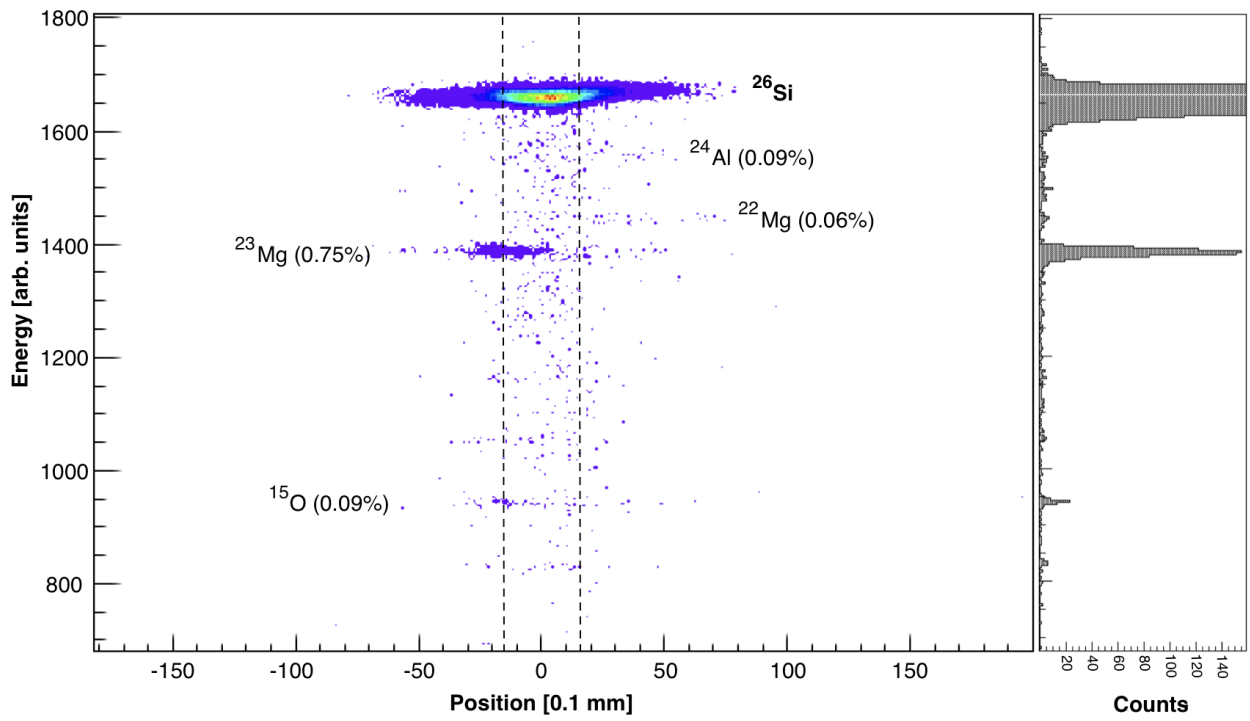

Figure 3.2: The deposited energy versus position as obtained with the PSSD in the MARS focal plane. The dashed line shows the position of the extractions slits, 3.2 mm apart, used during this measurement. The projection on the right shows the intensity of ^{26}Si and the impurities with the slits in place.

3.2 Fast tape-transport system

We use the fast tape-transport system at the end of the MARS focal plane to move the sources collected on the aluminized mylar tape to a well-shielded counting area. The system consists of two reels mounted on two separate decks. Each tape deck has its own vacuum buffer and controls; the height of each deck is adjustable by motor drive. The tape-transport system operates entirely in air for use with the relatively energetic radioactive beams extracted from MARS. A source is implanted when the tape is stationary. After a preset time the tape is rapidly moved to a counting location. The tape leaves a reservoir reel (on Deck#2) by being engaged by a pinch roller located on the take-up reel deck (Deck #1 in Figure 3.3); when the pinch roller presses against a capstan rotating at a regulated 3800

rpm it is guided from the collection position to the counting location as the tape is wound on the take-up reel. Two brakes are located, one on each side of the counting location, to stop the tape promptly and stretch it tightly in front of the detectors. Air bearings are installed along the horizontal path to ensure that the tape moves with the least amount of friction. The distance that the tape moves is determined by the pre-set time between the engagement of the pinch roller and the closing of the brakes. Both ends of the tape have a clear section where the aluminum has been chemically removed from the tape. When the clear section is detected by optical sensors the tape rewinds and the cycling automatically restarts after the rewind is completed. The collect/move/count times can be set to suit depending on the experiment and the isotope being measured. The times are initially set on the control panel on one of the decks and later can be changed remotely for fine tuning. The fast tape-transport system was build almost 20 years ago and has proven to be a reliable mechanism for precision measurements of the half-life and branching ratios of radioactive isotopes.

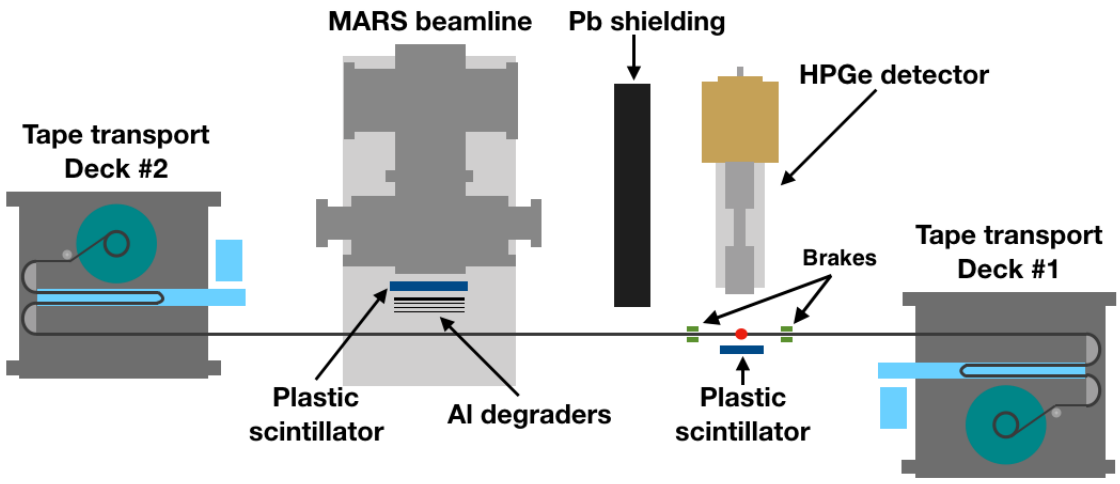

Figure 3.3: Schematic drawing of the experimental setup used for the branching ratio measurement of ^{26}Si.

3.3 Data acquisition system

The data acquisition system developed at the Cyclotron Institute at Texas A&M University for this type of measurement is based on KmaxNT software [23] and on CAMAC modules with FERAbus (Fast Encoding and Readout ADC) capability. The acquisition system introduces essentially no extra dead-time relative to that of the digital converters. The system hardware includes a CAMAC controller with SCSI capability, a FERA driver, two dual port FERA/CAMAC buffer memories, three types of converters [Analog-to-Digital Converter (ADC); Charge-to-Digital Converter (QDC); Time-to-Digital Converter (TDC)] and a PC with Windows NT operating system. In order to achieve the best timing and energy resolution for coincidence measurements, the signals are split into two from each detector, one associated with time and the other one associated with energy. These signals are processed separately and the results are then combined. More information on the acquisition system can be found in [24]. For a branching ratio measurement, the time-tagged β-γ coincidence data is recorded event by event. Other recorded quantities are the β and γ-ray energies, the coincidence time between β and γ, the total number of β-singles, and the time the event occurred after the beginning of each cycle. A diagram of the data acquisition system is shown in Figure 3.4. The schematic shows the main electronic components used to process the heavy ion, β, and γ signals.

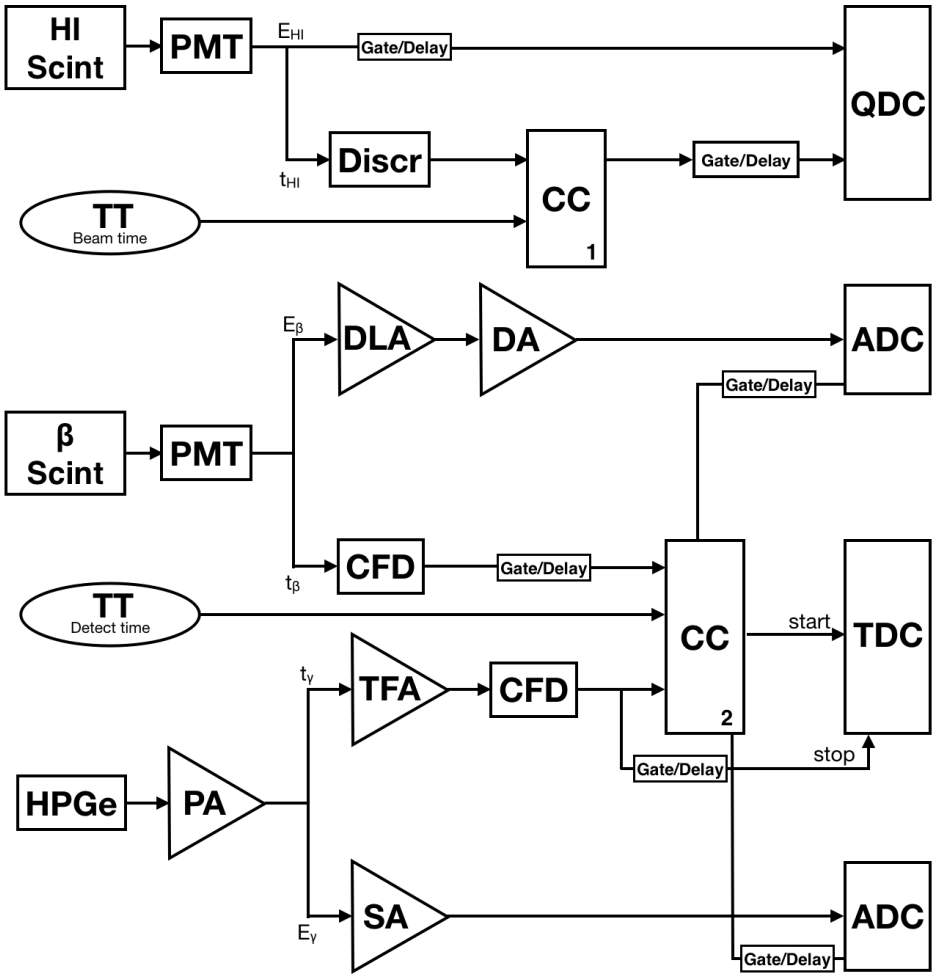

Figure 3.4: Schematic diagram of the data acquisition system used to measure the branching ratio of ^{26}Si. HI Scint, heavy ion scintillator; β Scint, beta scintillator; HPGe, high purity Germanium detector; PMT, photomultiplier tube; PA, pre-amplifier; TT, tape transport; Discr, discriminator; DLA, delay line amplifier; CFD, constant fraction discriminator; TFA, timing filter amplifier; SA, spectroscopy amplifier; CC, coincidence unit.

3.3.1 Detectors

For this particular experiment a 1-mm thick BC404 plastic scintillator was placed close to the aluminized mylar tape for the detection of β particles. The actual distance was measured to be 1.55 mm from the tape to the thin Havar window of the detector (see Section 3.4), with the plastic scintillator located 1.9 mm behind that window. Our β detector consists

of a Bicron BC404 scintillator disk recessed into a cylindrical Lucite light guide, which is coupled, in turn, to a photomultiplier tube. Its fast time response, energy proportionality and insensitivity to γ radiation makes it ideal for β singles and β-γ coincidence measurements. The response function for the β detector has been characterized using conversion-electron sources and Monte Carlo calculations [25, 26]. While a Si detector has similar properties for the detection of β particles it is more sensitive to the detection of γ rays, which presents a problem for precision measurements. Also it needs a cooling system and cannot operate in air.

In the case of γ rays a high-purity germanium (HPGe) detector was used. The HPGe detector is a coaxial type with an active volume of 280 cm^3 made from n-type Ge semiconductor. It is quoted by the manufacturer as having 70% efficiency for 1.33 MeV γ-rays relative to a 3" $\times$ 3" NaI(Tl) crystal. The detector is placed on the opposite side of the tape, 15.1 cm away, the distance for which the detector has been meticulously calibrated using 13 individual sources from 10 different radionuclides (^{48}Cr, ^{60}Co, ^{88}Y, ^{108m}Ag, ^{109}Cd, ^{120m}Sb, ^{133}Ba, ^{134}Cs, ^{137}Cs, ^{180m}Hf) [27]. The relative and absolute efficiency measurements combined with Monte Carlo calculations provide us with an uncertainty of $\pm$0.2% in the efficiency curve between 50 and 1400 keV [27] and $\pm$0.4% between 1400 and 3500 keV [28]. The HPGe detector has been ,and continues to be, kept at liquid nitrogen temperature at all times to preserve the calibration.

3.4 Branching ratio measurement of ^{26}Si

The branching ratio measurement of ^{26}Si was performed using the methods, hardware and software described in the previous sections. A ^{26}Si beam separated from the primary beam by MARS was used. The data were collected in repetitive cycles. First, ^{26}Si was collected in the tape for 5 s, where the rate of accumulation was measured by a BC-404 scintillator located at MARS exit. Afterwards, the beam was interrupted and the tape moved for 160 ms to the well-shielded counting location, about 90 cm away, where time

tagged β-γ coincidence events were measured by the 1-mm-thick plastic scintillator and HPGe detector. After 5 s, when the counting was completed the beam was restored and the cycle repeated. During the seven-day run over 25,000 cycles were repeated to accumulate, approximately, 13 million β-γ coincidence events, 527 million β singles and 53 million γ events. As mentioned in the previous section, the plastic scintillator detector at the counting location was placed with its window at a distance of 1.55 mm from the tape and the HPGe detector was 15.1 cm away on the opposite side of the tape. The distance between tape and HPGe was measured during every cycle with a laser triangulation device that allowed us to determine the source-to-detector distance with an accuracy of $\pm$0.1 mm as specified by the manufacturer [29]. The distance from the tape to scintillator window was measured using this same laser triangulation system by removing the tape and obtaining the laser reading to the Havar window. Knowing the distance of the HPGe detector to tape and HPGe detector to Havar window we can subtract to obtain the tape-to-window distance, taking account of the appropriate angle.

During the measurement our data-acquisition system generated a master trigger by identifying the arrival of a β particle and a γ ray within 2 μs of one another (CC 2 in Figure 3.4). This signaled the occurrence of a potentially coincident β-γ event and initiated acquisition. For each such event, the energy of both the β and the γ rays, the precise ($\pm$1 ns) time difference between their arrivals, and the time when the event itself occurred relative to the beginning of the counting period were recorded. The time-difference spectrum was later used to separate real from random coincidences. For each cycle we also recorded the rate of accumulation of ^{26}Si ions in the tape as a function of time during the collection period; then the total number of β and γ-ray singles, and the laser distance readings during the counting period. The same discriminator signals used to scale the β singles were also used in creating the master triggers, which established the occurrence of potential β-γ coincidences.

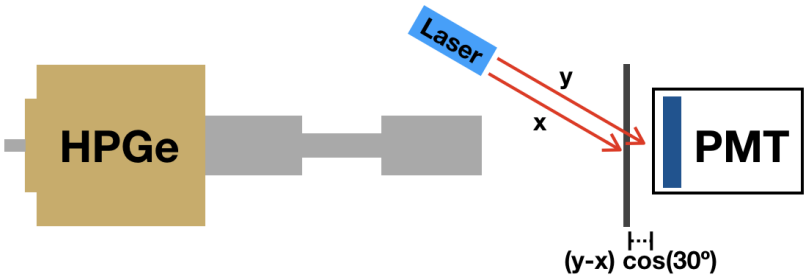

Figure 3.5: Schematic diagram for the tape to scintillator Havar window distance measurement.

4. EXPERIMENTAL ANALYSIS

The decay of ^{26}Si offers a superallowed branch, which feeds the 228-keV isomeric state of its daughter ^{26m}Al, as well as competing Gamow-Teller branches to higher excited 1^+ states, each of which is followed by the emission of a γ ray to the isomeric state. The simplified decay scheme is shown in Figure 4.1. The branching ratio is a measure of the partial β^+ transition probability to a particular daughter state as a fraction of the total transitions from the parent state. Since the superallowed branch in this particular decay is not followed by a γ ray, the branching ratios can only be determined if we know the absolute γ-ray intensities. The β-γ coincidence technique is a powerful way to achieve this goal [30]. In order to obtain the branching ratio to the superallowed state we first need to determine the absolute branching ratio to the most intense 1^+ branch. From the relative intensities of all the other γ-ray peaks we can next determine the Gamow-Teller branching ratio to all 1^+ states in ^{26m}Al. Subtracting this total from 100% we can obtain the branching ratio to the 0^+ state, which itself emits no prompt γ-ray.

$$R_F = 1 - \Sigma R_i \tag{4.1}$$

where R_F represents the branching ratio for the superallowed state or Fermi branch and R_i the branching ratio for population of a particular excited state, i, that decays by emitting a γ ray.

The fact that the observed transitions from ^{26}Si sum to a relatively small value, 25%, works to our advantage when trying to achieve the precision required to make this measurement relevant for our goal of reducing the uncertainties in the ft-value and subsequently for the ft mirror ratio. Since the superallowed transition is determined by subtracting the Gamow-Teller transitions from 100% the fractional uncertainty from the result will be reduced by a factor 3.

The first step to determine the branching ratio to the 1^+ state in ^{26m}Al at 1058 keV is accomplished by obtaining the number of β-coincident 829 keV γ rays relative to the total number of positrons emitted from ^{26}Si. More specifically, to determine the branching ratio, R_i, for a β^+ transition populating a particular state i, which is deexcited by the emission of a γ ray, γ_i, we relate the number of γ-rays observed in coincidence with β-particles at the counting location, $N_{\beta\gamma}$, to the N_β-singles rate, N_β:

$$N_{\beta\gamma} = N_{decays}\epsilon_{\beta_i}\epsilon_{\gamma_i}R_i, \tag{4.2}$$

$$N_\beta = N_{decays}\epsilon_\beta, \tag{4.3}$$

the ratio of these two quantities is then,

$$\frac{N_{\beta\gamma i}}{N_\beta} = \frac{\epsilon_{\beta_i}\epsilon_{\gamma_i}R_i}{\epsilon_\beta}. \tag{4.4}$$

Solving for R_i we then obtain the branching ratio equation:

$$R_i = \frac{N_{\beta\gamma i}}{N_\beta \epsilon_{\gamma i}}\frac{\epsilon_\beta}{\epsilon_{\beta i}}, \tag{4.5}$$

where, experimentally, $N_{\beta\gamma i}$ is the total number of β-γ coincidences in the γ_i peak, N_β is the total number of β singles corresponding to ^{26}Si, ϵ_i is the efficiency of the HPGe detector for detecting γ_i rays, $\epsilon_{\beta i}$ is the efficiency of the plastic scintillator for detecting the β's that populate state i, and ϵ_β is the average efficiency for detecting β's from all ^{26}Si transitions. This branching ratio result is then multiplied by factor k_i that accounts for small experimental corrections discussed in later sections and summarized in Section 4.6. The weaker transition intensities can then be obtained from the relative intensities of the γ-ray peaks.

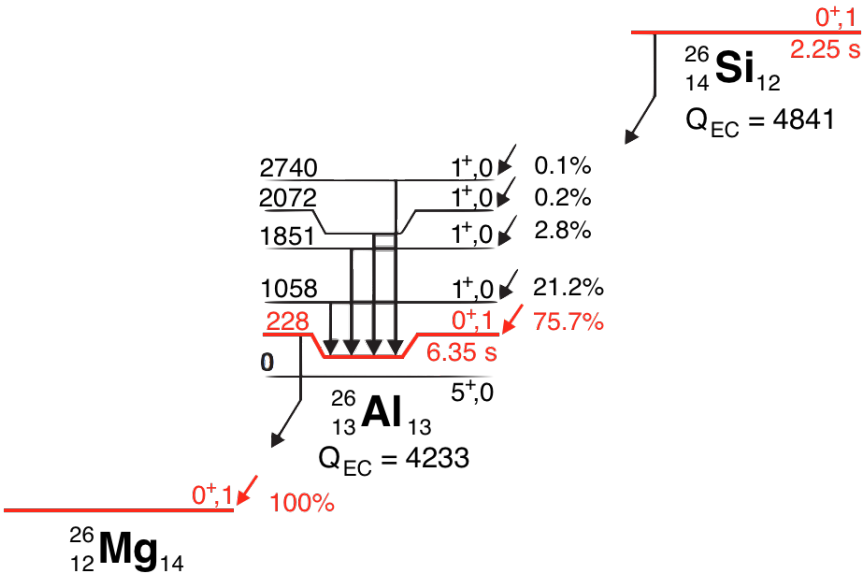

Figure 4.1: Decay scheme of ^{26}Si showing the four strongest branches and the most intense subsequent γ-ray transitions in ^{26m}Al. All energies are in keV and the Q_{EC} values shown are for the superallowed branches which are shown in red.

4.1 Data selection

From the ∼26,000 cycles collected during the experiment only those that met certain criteria were used. This criteria takes into account errors associated with the mechanics of the tape transport system 4.2. The first criterion used for filtering was the number of implanted ^{26}Si ions as detected by the BC-404 scintillator at the exit of MARS. The cycles accepted were those with a collection rate between 2,000 and 34,000 ions/s. This removed cycles with no beam and those with abnormally high beam currents. The second criterion was the ratio of the number of beta particles detected to the number of ^{26}Si ions implanted. Setting this filter to reject anomalously low values, less than 85% of the maximum value, allowed us to reject cycles in which the tape transport system did not move the sample to the central position between the β detector and HPGe detector (see Figure 4.3).

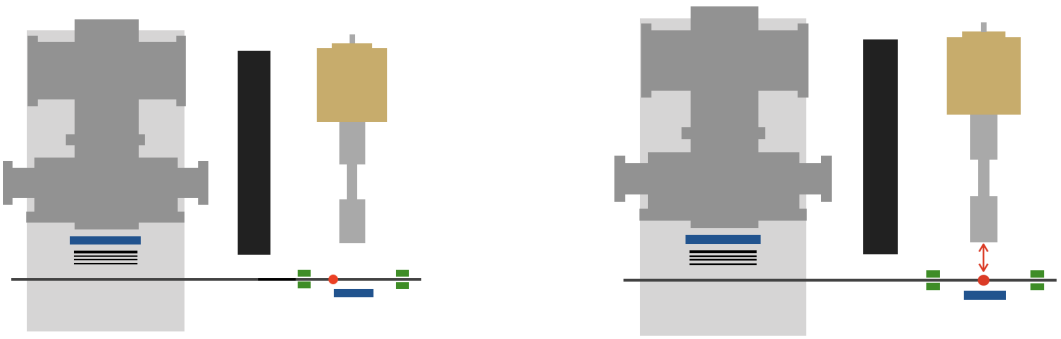

(a) Transversal position.

(b) Longitudinal position.

Figure 4.2: Diagrams showing the different criteria used for source positioning; (a) shows a source missing the central location ‘along the transversal axis of the tape transport system, while (b) shows the distance from tape to detector.

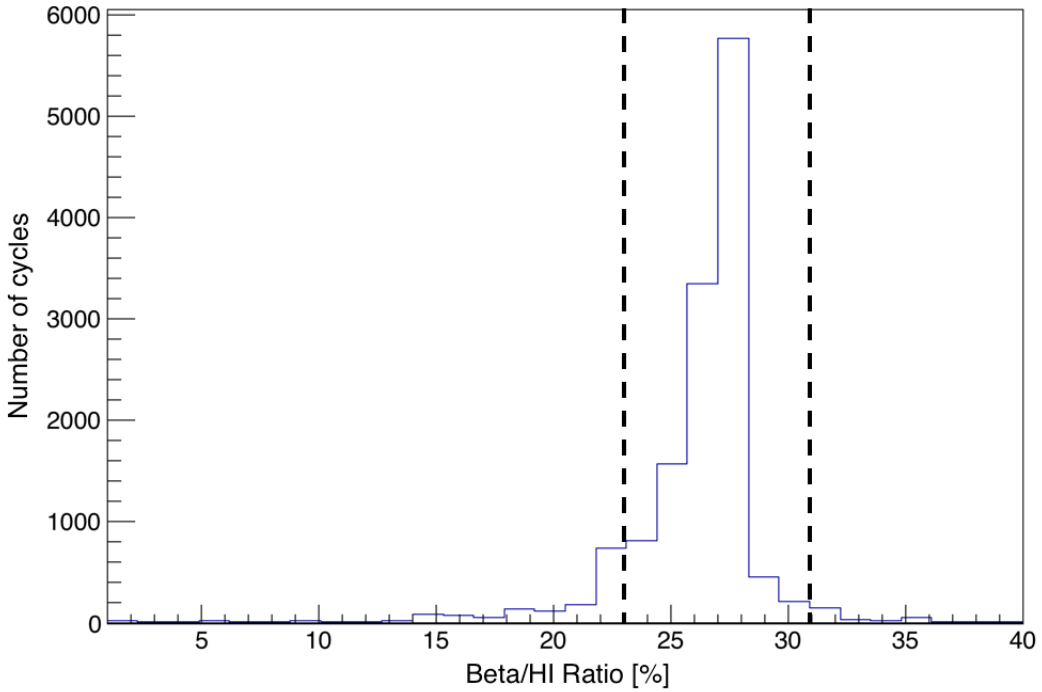

Figure 4.3: Beta-to-HI distribution for all cycles. The dashed lines represent the limits for selection.

When the sample is not moved to the appropriate position it affects the efficiency of both the beta and gamma detectors. To illustrate this, a measurement to determine the geometrical efficiency of the β detector was done, and the results are shown in Appendix B.

For the third and final filter, we rejected cycles where the distance between the HPGe detector and the tape is not within the narrow position distribution (Figure 4.4). This filter is applied based on the reading of a laser sensor mounted next to to the HPGe detector which takes a reading for every cycle. This filter allows us to take full advantage of the precise calibration of the detector. Out of 25,736 cycles recorded, 132 of them were rejected by the HI filter, 2,105 by the β/HI ratio criterion and 69 were removed based on their position. After the selection was done, 23,430 cycles (92%) of the total remained and this is the data set that were used for the rest of the analysis.

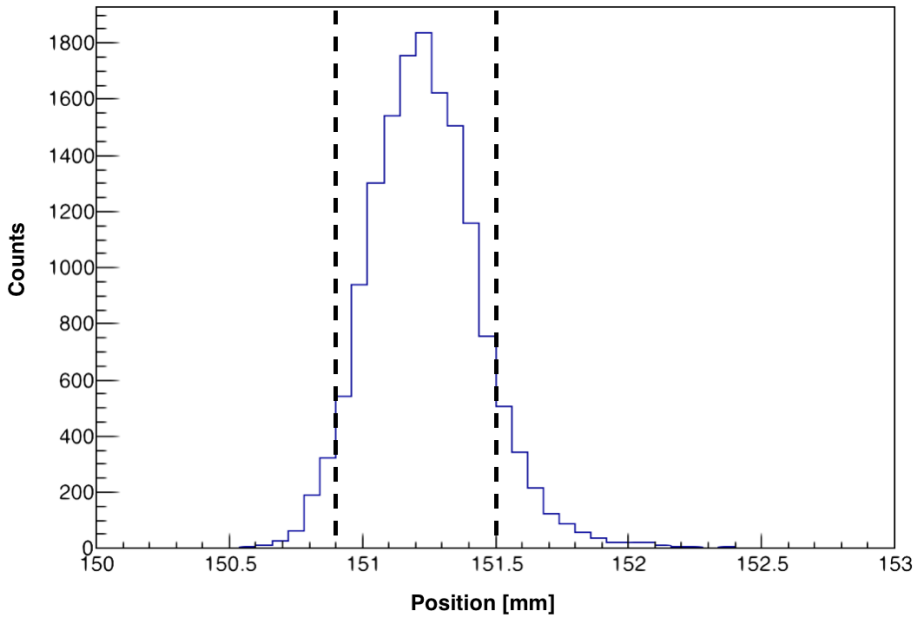

Figure 4.4: Position distribution for all cycles as measured by the laser sensor

During the analysis process we found that the collected data could be divided into three

evenly split groups based on the counting rate of β's during a cycle. Since different rates affect some experimental corrections differently (*i.e.* dead time) three different numbers will be presented for those corrections that require it. For simplicity the three regions have been labeled Low, Med and High according to their rate. Figure 4.5 shows the beta rate distribution as well as the limits for each one.

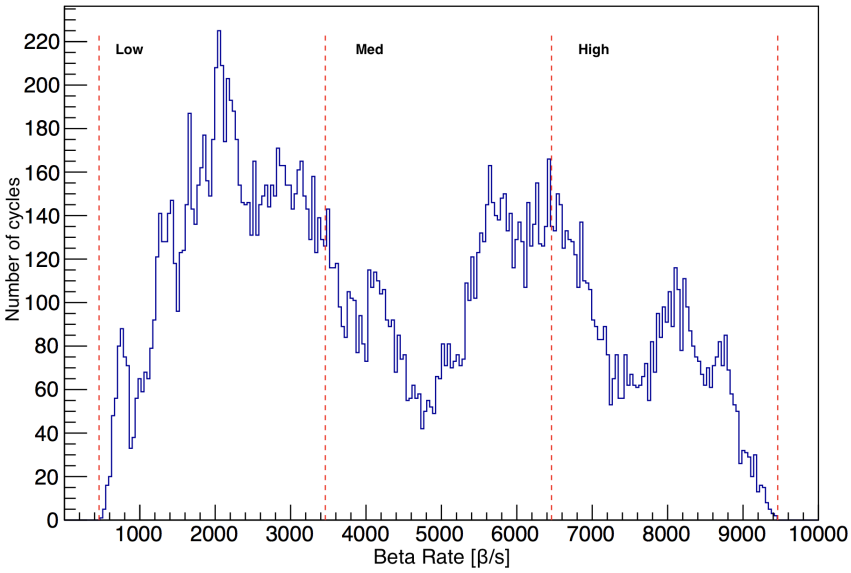

Figure 4.5: Beta rate distribution for all cycles. The red lines represent the limits for each set at 460, 3460, 6460 and 9460 for an even split of 3000.

4.2 γ-ray intensities

When measuring β-γ coincidences there is a a finite probability that two separate events from independent decays occur closely spaced in time and are counted as a coincidence. This can be corrected since we recorded the time between the detection of a γ ray and the subsequent arrival of an electronically delayed signal from the positron. The TDC-gamma 2D spectrum for all events is shown in Figure 4.6. From this spectrum we are able to project onto the x-axis to obtain a gamma spectrum (Figure 4.7) and to the y-axis to obtain a time spectrum (Figure 4.8). The broad peak corresponds to real coincidence events while the flat

regions on both sides correspond to random coincidences. The prompt peak has a noticeable tail to the left, this occurs because it includes all coincidence events which means the full range of γ-rays is present. Lower energy γ rays trigger the TDC later than high energy ones which results in longer times before the arrival of the corresponding β particle.

From this time spectrum we could produce a γ-ray spectrum free of random coincidence events by obtaining β-γ spectra gated either on the prompt peak or on the flat parts of the spectrum. The γ-ray spectrum obtained from the flat regions can be normalized and then subtracted from the prompt-peak gated spectrum, giving as a result a random-coincidence-free spectrum where all peaks belong to the decay of ^{26}Si. The spectrum shown in Figure 4.9 has already been corrected for random coincidences.

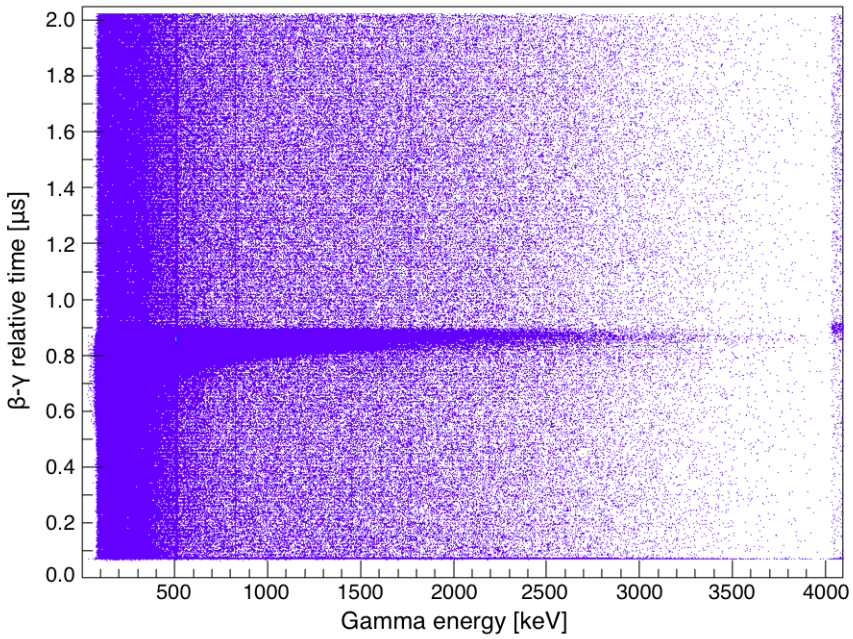

Figure 4.6: 2D spectrum showing coincidence events with their respective gamma energies as well as the time difference between the arrival of β-γ coincidence pairs.

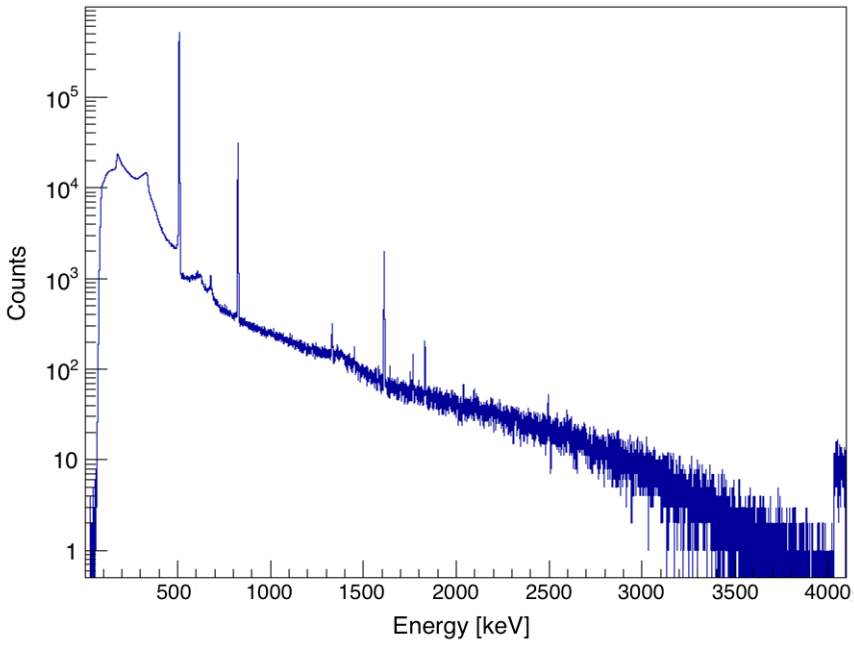

Figure 4.7: Full gamma spectrum projection not corrected for random coincidences.

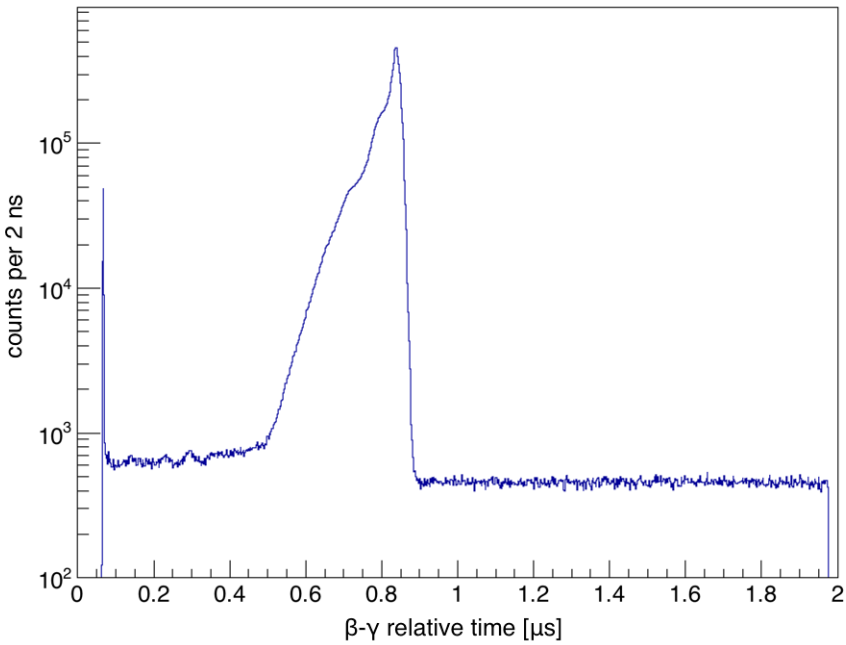

Figure 4.8: Measured time difference between the arrival of a γ ray and its corresponding β particle for all coincidence events.

From Eq. 4.5 we see one of the quantities needed is $N_{\beta\gamma}$. It can be obtained from the γ-ray spectrum in coincidence with betas shown in Figure 4.9. In this spectrum we can see a prominent 511 keV γ-ray peak produced by positron annihilation, the four gamma rays of interest from the 1^+ states in ^{26m}Al (829 keV, 1622 keV, 1843 keV and 2511 keV), as well as two sum peaks; the "511 + 171" peak corresponds to the sum of two annihilation photons one of which was backscattered; and the "511 + 829" peak results from the summing between the 829 keV γ and the annihilation radiation from positron decay.

To determine $N_{\beta\gamma}$, the areas of all γ peaks were analyzed using GF3, a least-squares peak-fitting program in the RADWARE [31] package. GF3 fits each peak with 3 components: A Gaussian, usually the main component, arising from complete charge collection of a photoelectric event in the detector; a skewed Gaussian, arising from incomplete charge collection; and a step function accounting for 2 effects: γ rays that Compton scatter outside the detector leading to secondary photons that enter the detector with reduced energy. The second effect is coming from γ-rays which have the appropriate energy to be within the energy peak, but deposit less than its full energy into the detector and thus is detected at a lower energy value. At energies higher than the energy peak, this cannot happen and therefore the background follows a step function. The first effect dominates at lower energies and the latter at high energies.

A Gaussian peak with a smoothed step function and a linear background in the peak region were sufficient to properly describe the data in the spectrum. The spectrum shown in Figure 4.9 shows the sum of all three rate-selected groups for a better visualization of the weaker γ-ray peaks while Figure 4.10 and Figure 4.11 shows the GF3 fit for the 829-keV peak from this spectrum and the output for that particular fit respectively.

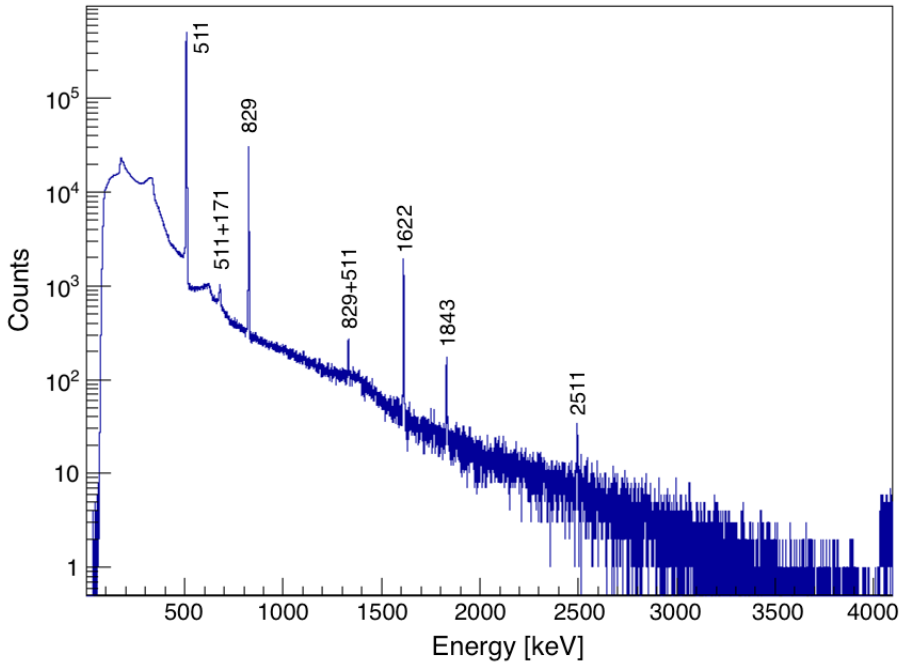

Figure 4.9: Spectrum of β-delayed γ rays observed in coincidence with positrons from the decay of ^{26}Si.

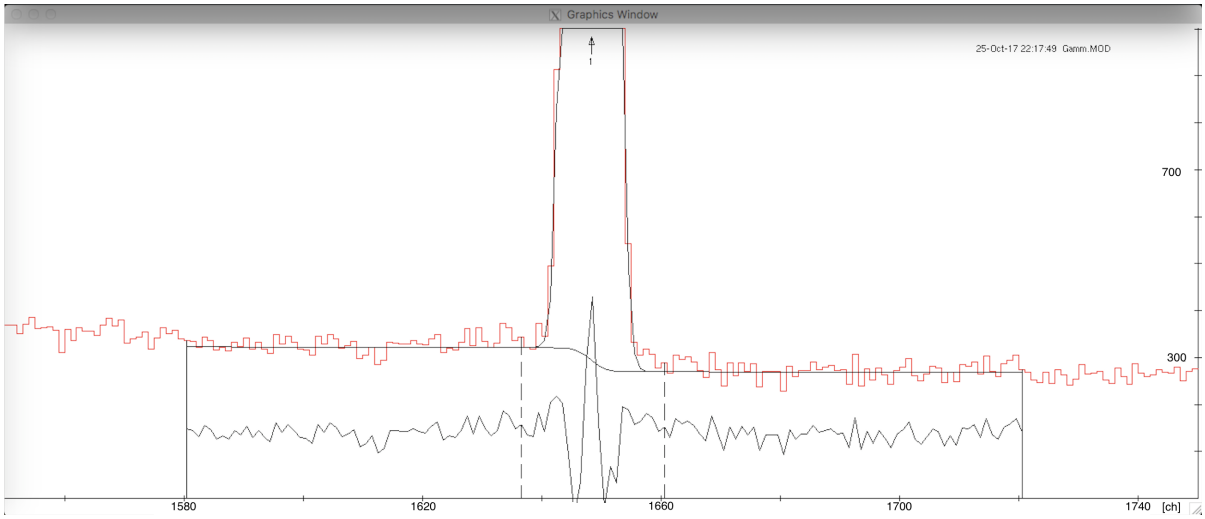

Figure 4.10: Sample fit using GF3 peak-fitting program for the 829-keV peak from the summed spectrum of all three rate-selected groups. The difference between the fit and the spectrum is shown between the spectrum and the x-axis with a vertical offset added to the difference for visibility reasons [31].

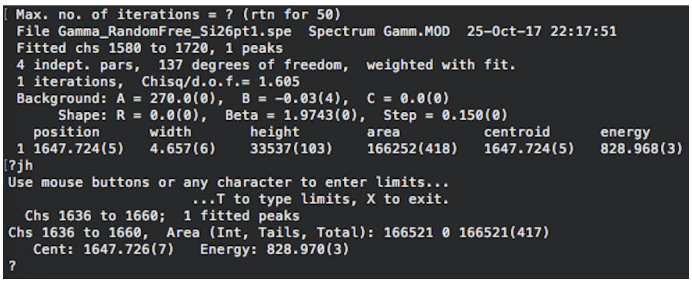

Figure 4.11: GF3 output for the fitting routine with a $\chi^2/\nu = 1.605$. A linear background $(A + Bx + Cx^2)$ was used by setting the C parameter to equal to zero and the step function determined by the energy.

The output of the fitting routine shows a large χ^2/ν which is typical since the fit is a true Gaussian function while the response function of the detector is not. This effect can be seen from the residuals in Figure 4.10. The quality of the fit for the peak itself is not as important as defining the background properly. With a properly defined background, the area of the peak was determined by the number of counts above the fitted background in the region limited by the dashed vertical lines. The experimental results for the areas of the peak of interest, 829 keV, for the three rate-selected groups appear in Table 4.1. The areas in the table below were obtained using the same fitting procedure as Figure 4.10. Since the data had to be split into three groups, a more extensive analysis of these peaks was done with various background limits. As can be seen from the fit mentioned before, a wide background was used to determine the background properly; however a narrower background was also fitted to make sure that the peak and its tails were not affected significantly by the choice. While both areas agree with each other by a fraction of their statistical uncertainty, the Med and High regions seemed to fit better with a wide background while the Low region was favored by the narrow one. The three areas presented were obtained from "weighted" average favoring the best fit and the uncertainties adjusted for it by $\sqrt{\sigma^2 + (weigth \times \Delta)^2}$, where Δ is the difference between peak areas using different background selection.

		Uncertainty		
Section	Peak area	Total	Statistical	Systematic
Low	34705	238	190	143
Med	63223	279	256	111
High	68719	304	267	145

Table 4.1: Random coincidence corrected peak areas for 829 keV γ ray.

4.3 β singles

Another quantity needed for the branching ratio equation (Eq. 4.2) is the total number of β particles emitted by ^{26}Si. Since the number of β particles recorded originate not only from the decay of ^{26}Si but also from its daughter ^{26m}Al as well as from impurities and background, some important corrections need to be taken into account.

4.3.1 Impurities

Based on the results obtained from MARS position-sensitive silicon detector, we can determine the surviving impurities, and using the SRIM [32] code we calculate the energy loss of these impurities as they pass through the plastic scintillator and Al degraders. From this we can then determine the amount of impurities collected in the tape so we can correct the total number of β particles accordingly. Some SRIM calculations were done beforehand to determine the amount of Al needed in order to stop the ^{26}Si in the middle of the tape (57 μm) and this thickness adjusted (to 146 μm) during the experiment to implant the isotope towards the back of the tape. This procedure was done with an automatic degrader changer designed for this specific task using stepping motors and Arduino microcontrollers [33] interfaced with "Processing" software [34] (see Appendix A for detailed description of the changer). The final thickness chosen for the Al degrader was determined after we performed

a "degrader scan". The degrader scan consists of using different degrader thicknesses and measuring the β to HI ratio for each setting. The results of the scan allowed us to confirm experimentally the results obtained from the SRIM calculations. Figure 4.12 shows the results from the degrader scan performed during the experiment; the thickness of the Al degraders is given in mils (1 mil = 25.4 μm) while β/HI is given as a percentage.

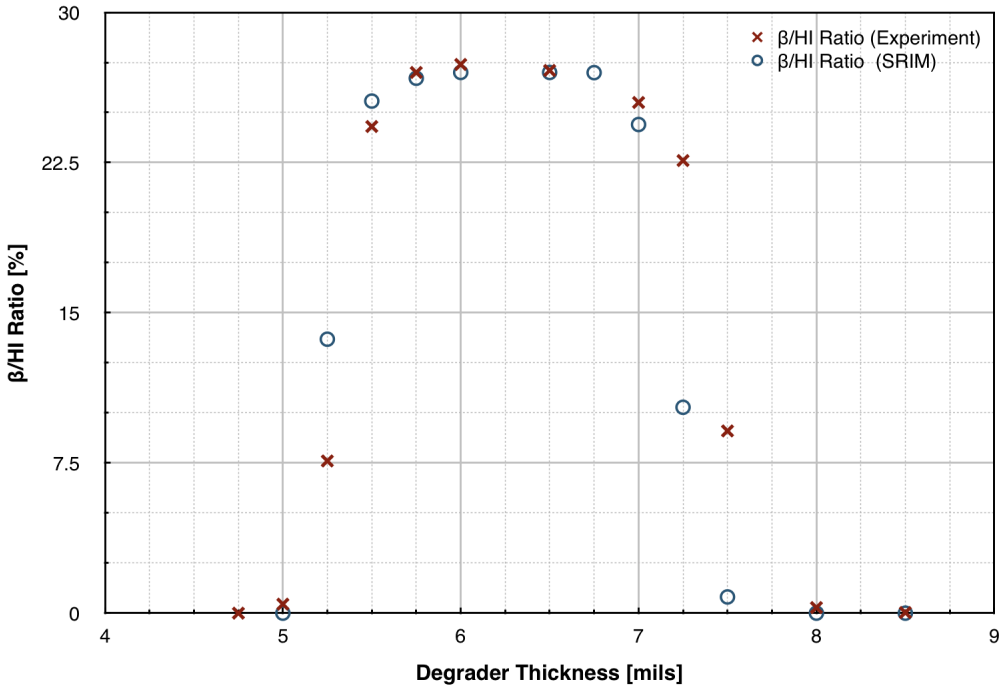

Figure 4.12: Degrader scan used to determine the appropriate Al thickness for proper beam implantation. Error bars are smaller than the data points.

The results of the scan showed that the thinnest degrader setting lets the beam punch through the tape, while the thickest degrader options completely stopped the beam from reaching the tape. Figure 4.13 shows the different implantation depths for ^{26}Si as well as the surviving impurities that can be implanted, ^{23}Mg and ^{24}Al, for four different settings. It is worth noting that the SRIM simulations give a very precise implantation location for a particular isotope, which looks similar to a delta function, due to the unchanging energy

of the simulated particles. In reality all these isotopes do not have the same energy but a range of energies which can be calculated using the MARS momentum spread. Using this momentum spread, the energy fluctuation was calculated and used in SRIM to determine the width of the implantation profiles displayed in Figure 4.13. The rectangular implantation profile was then convolved with a Gaussian function ($\sigma = 2$) to obtain the tailing of the implantation resembling a real-world scenario. To determine the width of the Gaussian, the degrader scan was fitted first using a trapezoidal function and a Gaussian function of varying width, once the proper width was found and the data properly fitted, the same width was use for the implantation profile.

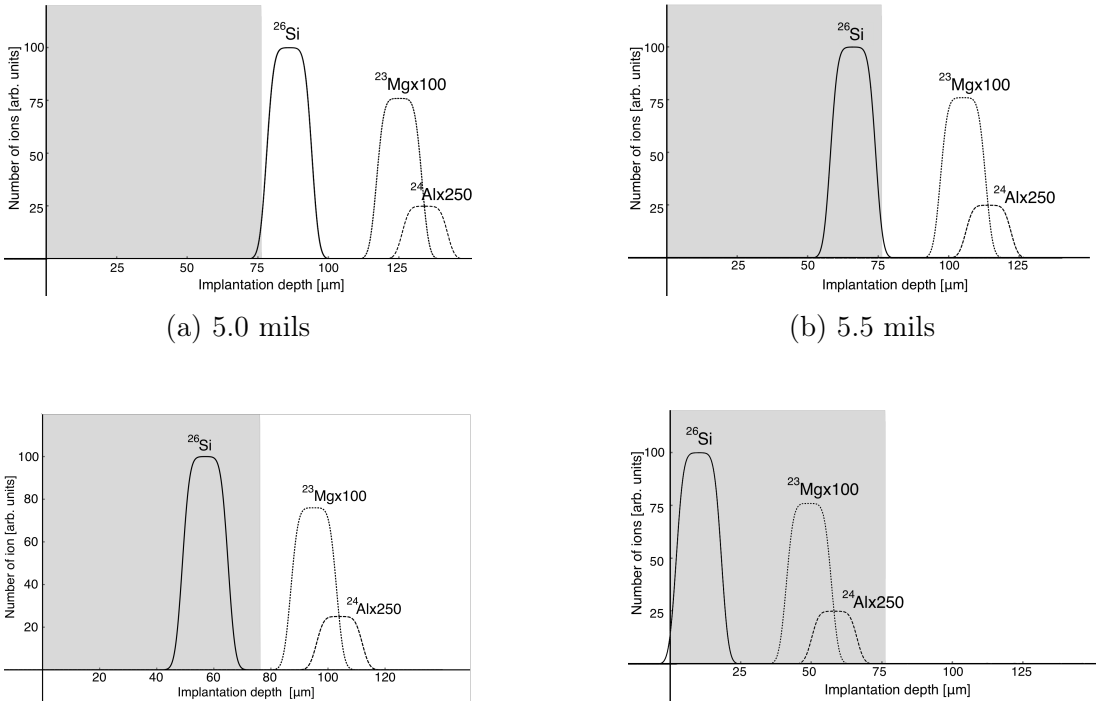

(a) 5.0 mils

(b) 5.5 mils

(c) 5.75 mils

(d) 7.0 mils

Figure 4.13: This illustration shows the implantation profile of the ^{26}Si beam and the surviving impurities in the mylar tape. The gray region corresponds to the actual thickness of the tape. The ions within this region are collected in the sample. All beams enter from the left.

Comparing these implantation profiles with the results from the degrader scan, it can be seen that 5 mils of Al lets most of the beam punch through which explains the low β/HI of 0.45%. With 5.5 mils, most of the ^{26}Si is implanted (β/HI = 24.3%) while the impurities punch through. Similarly, using 7 mils of Al, deposited approximately the same amount of ^{26}Si, this time towards the front of the tape, however, it also allowed the impurities to be fully implanted which raised the β/HI value to 25.5%. After we had performed a full scan we chose the setting to be 5.75 mils (146 μm); thus, the impurities that survived the MARS filtering procedure punched through the tape and did not have any effect on our measurement, as seen in Figure 4.13(c). If we consider the case where the Al degrader setting is 6.0 mils instead of 5.75, then 1.25% of the ^{23}Mg (0.75% relative to ^{26}Si) gets implanted on the tape. Knowing the half-life of this impurity to be 11.317 s, we calculated the correction for this scenario to be 5.51×10^{-5}, which serves as an upper limit to the contributions that impurities might have. A careful analysis of the γ-ray spectrum was done and no γ rays associated with any of the impurities were found. This did not come as a surprise based on the quantity of impurity produced and their most intense γ rays: ^{23}Mg (439.98 keV, 8.2%) and ^{24}Al (1368.62 keV, 96.0%).

4.3.2 Parent-daughter β-decay fraction

As data were being collected ^{26}Si was decaying into ^{26m}Al, which also decays into ^{26}Mg. This means that the number of β-singles we detect includes both the decay of the parent nucleus and a fraction of the decay of the daughter. This is important so that we can determine the total number of β-singles corresponding to ^{26}Si. Knowing the half-life of both isotopes, ^{26}Si and ^{26m}Al, [1, 5, 35] as well as the time profile of heavy ions implanted on the tape, which are recorded during the experiment, we can determine the activities of both and we can obtain a ratio.

The contribution of the daughter nucleus to the number of beta singles is by far the largest correction to N_β, but a straightforward one. During the 5-s collection time for each

cycle, the scintillator located at the MARS exit measures the rate at which ions are being accumulated in the tape. Figure 4.14 shows the cumulative beam profile for all selected cycles.

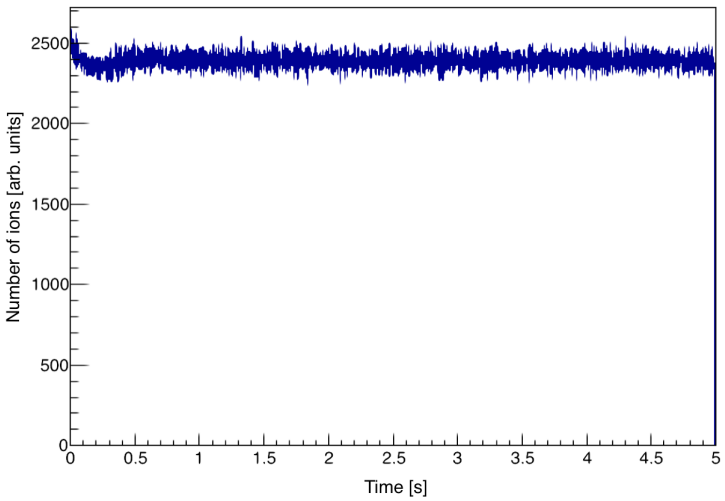

Figure 4.14: Beam time profile collected during the entirety of the run. The initial drop in intensity is generated by the decrease in local density of the hydrogen in the target cell as the primary beam heats the gas around its path. A fan located inside the gas target mitigates the effect and ensures a rapid transition to stable conditions.

The rate of implantation is recorded in 4000 intervals of 1.25 ms, allowing us to numerically calculate the amount of ^{26}Si that decays into ^{26m}Al and its subsequent decay into ^{26}Mg using the standard exponential decay equation (Eq. 4.6) and a slightly modified one to account for a continuous flux of ions, Φ, during the collect time (Eq. 4.7):

$$\frac{dN}{dt} = -\lambda t \implies N(t) = N_0 e^{-\lambda t}, \tag{4.6}$$

$$\frac{dN}{dt} = \Phi - \lambda t \implies N(t) = \frac{\Phi}{\lambda}(1 - e^{-\lambda t}), \quad N(t=0) = 0. \tag{4.7}$$

Although we do not have a constant flux of ions (as seen from Figure 4.14), the decay

of both parent and daughter were completed on a channel by channel basis, meaning that during the 1.25 ms intervals used, the beam profile can be thought of as constant. Figure 4.15 shows the activity of the parent and daughter as a function of time. It can be seen during the collection time that there is a rapid increase in the activity of ^{26}Si and as a consequence an increase in the activity of the daughter as well, both due to the almost constant flux of ions coming out of MARS during this period. After calculating the ratio of activities it was determined that 56.91% of the β-singles recorded are produced by the decay of ^{26}Si. This fraction remains the same regardless of the β rate.

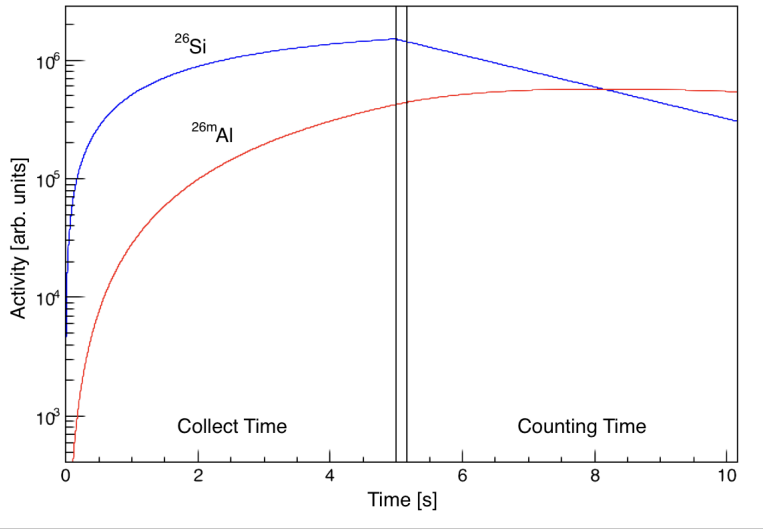

Figure 4.15: Activities for ^{26}Si (blue) and ^{26m}Al(red) shown as a function of cycle time.

4.3.3 Background measurement

The room background was measured during the experiment in order determine the contribution to β-γ coincidence spectrum and β-singles rate. This was done by measuring cycles in which we disabled the tape transport system motion by disengaging the pinch roller: *i.e.* the cycling was maintained but the tape did not move the activity to the detector. All

other settings remained the same. Though very low, the β-singles rate from this background measurement was incorporated into the analysis. The background rate for β singles was 0.6 β/s about 3 orders of magnitude less than the β count rate during a measurement. We can now determine the number of β particles corresponding only to the decay of ^{26}Si.

4.3.4 γ rays in β detector

There is a very small probability that γ rays produced from the decay of ^{26}Si get counted in the β scintillator. This effect does not matter for annihilation radiation which can be thought of as equivalent to a β particle in contributing to a valid coincidence trigger; it does matter for all other γ rays when they get detected but the corresponding β feeding the transition is not. Using EGSnrc Monte Carlo calculations [36] this effect was determined to have an effect of 0.12%. We can now determine the number of β particles corresponding only to the decay of ^{26}Si.

4.4 Experimental corrections

Although we have already discussed several corrections relating in particular to the number of β particles resulting from the decay of ^{26}Si. This section will focus on explaining the rest of the experimental corrections which, like coincidence summing, can significantly affect the number of β-γ coincidences, or, like γ-ray counts on the β detector, can have a very small impact.

4.4.1 Real-coincidence summing

Since each 829-keV γ ray from the 1058 keV state in ^{26m}Al is accompanied by a positron from the ^{26}Si β^+-decay branch that populated the state, there is a significant probability that the 829-keV γ ray and the 511-keV radiation from positron annihilation will reach the HPGe detector simultaneously and be recorded as a single γ ray with a combined energy

of 1340 keV (refer to Figure 4.9). Any summing of this nature will steal counts from the 829-keV peak of interest. In order to account for this loss we need to begin with the area of the observed sum peak; however, the losses not only come from the summing with the full energy 511-keV γ ray but also from 511-keV photons that Compton scatter in the HPGe crystal and deposit less than their full energy (see Figure 4.16). To correct for all the missing counts, which are indistinguishable from the continuum, we multiply the sum-peak area by the measured total-to-peak ratio, R_{tp}, of our detector at 511 keV. The term total-to-peak ratio is used to refer to the ratio of the total counts recorded by the detector to the counts recorded in a peak associated with a specific energy. The equation for this correction can be expressed as:

$$N_{\gamma true} = N_{\gamma observed} + N_{sum} R_{tp} \tag{4.8}$$

where $N_{\gamma observed}$ is the area of the 829-keV peak, N_{sum} is the area of the sum peak, and $N_{\gamma true}$ the true area of the 829-keV peak.

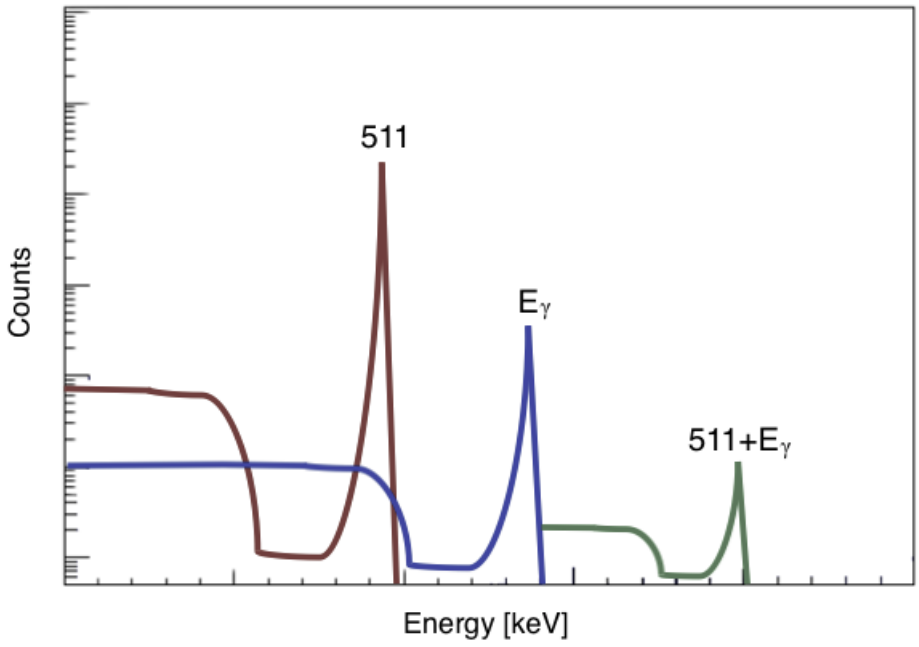

Figure 4.16: Sketch showing the underlying structure of the 511-keV peak (red) and that of an arbitrary peak (blue), E_γ, as well as the resulting sum peak (green), $511 + E_\gamma$.

The total-to-peak ratio was determined by a series of ^{68}Ge in-lab measurements as well as one made under experimental conditions. A ^{68}Ge source decays by electron capture to ^{68}Ga, which then decays into ^{68}Zn mostly by positron emission (Figure 4.17). It provides a γ-ray spectrum consisting of mostly 511 keV annihilation photons. The spectrum is shown in Figure 4.18. The lab measurements were done at the nominal distance of 15.1 cm with increasing amounts of shielding around the HPGe detector. The purpose of these measurements was not only to determine the total-to-peak ratio but also the impact of the detector shielding on that ratio. As shielding was added the greatest impact came with the first level of shielding, which consisted of a copper sleeve around the detector. Any extra shielding had minimal to no impact. To obtain the total-to-peak ratio, EGSnrc Monte Carlo calculations were used to determine the number of the γ rays below the cutoff energy of the detector, this lead to a ratio of 3.59. This result along with the sum peak area give us a 3.1% loss of 829 keV events due to summing with annihilation radiation. Real-coincidence summing is by far the largest correction in our analysis.

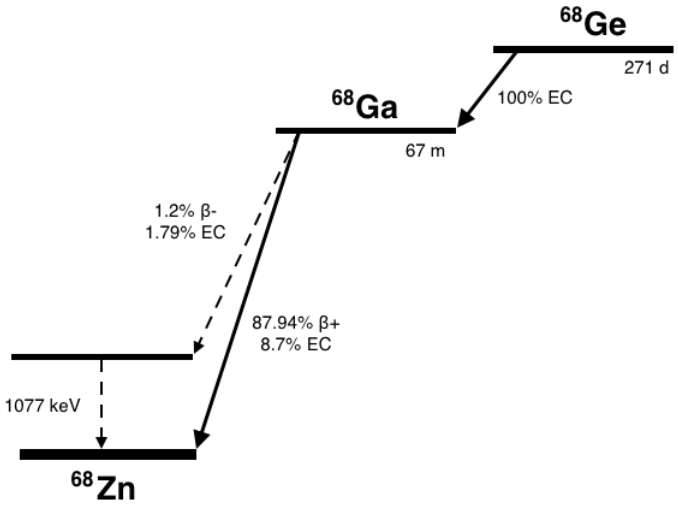

Figure 4.17: Simplified decay scheme for ^{68}Ge. All energies in keV.

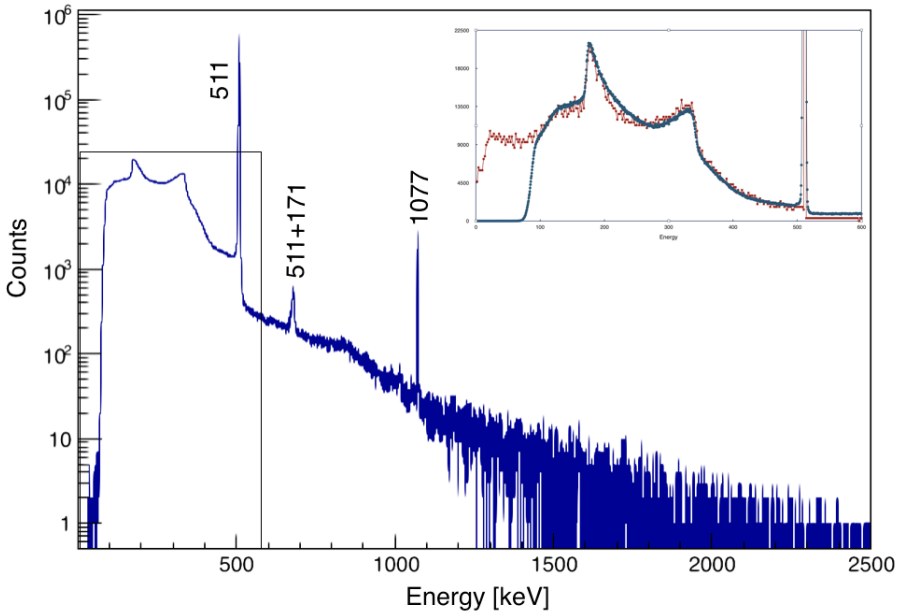

Figure 4.18: Gamma ray spectrum observed from the decay of ^{68}Ge under experimental conditions. The inner graph gives a closer look at the area specified by the frame where the simulation for the γ rays below the cutoff energy can be seen.

4.4.2 Dead time and pile-up

From Eq. 4.5 we can see that any dead time in the β-detection system will affect both numerator and denominator equally. Because of this and the fact that the dead time per event in this system is very small, 450 ns, it is considered no further. In contrast, the HPGe detector signals are much slower and are affected by dead time and pileup. The impact of these corrections depends on the rate of coincident γ rays as well as the γ singles rate. Since this correction is affected by rate, three corrections are needed for the three different data subsections presented in Figure 4.5. The dead time per event for encoded coincident γ rays was measured online and it also includes pileup time, 25.6 μs. This measurement was achieved by pulser signals from a constant frequency pulse generator measured in coincidence with gating signals from β-singles events, γ-singles events, and β-γ coincidence events. Because the total number of generated pulser events is known, the loss factor is simply the

ratio of recorded to generated pulser events. The γ singles pileup was determined from the signal pulse shape to be 17 μs. Both dead time and pileup remove legitimate signals. The calculated losses take into account the decrease in rate from the decay of ^{26}Si as well as the growth and decay of its daughter. The calculated corrections are listed in the table below. The results show the dependence on rate of this correction, with higher rates having a larger dead time correction.

Section	Dead time/pileup	Uncertainty
Low	1.0056	0.0070
Med	1.0111	0.0039
High	1.0160	0.0031

Table 4.2: Dead time/Pileup correction factors for the total number of β-γ coincidences.

4.4.3 Preemption of real coincidences

There is a small probability that coincidences are lost due to random coincidences preempting a real one. This occurs when the master trigger for our system is activated by a real β-γ coincidence opening a coincidence window but a random β event closes it before the real coincident β does. Figure 4.19 illustrates the difference between real coincidences, random coincidences and the preemption of real coincidences.

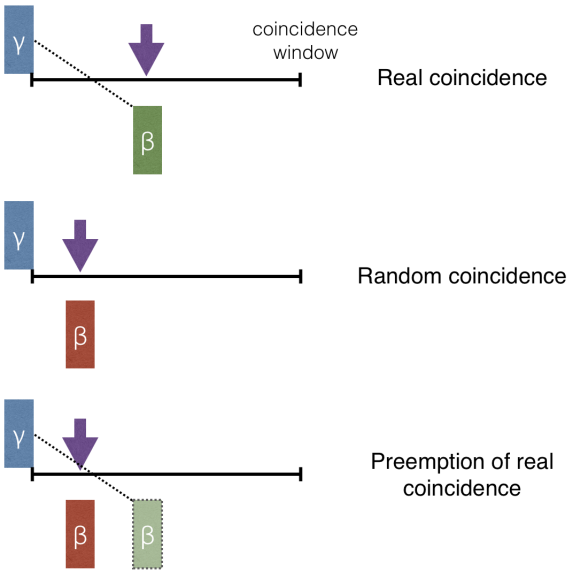

Figure 4.19: Difference between real, random and preemptive coincidences. The green blocks represent the β particle associated with the γ ray that triggers the coincident window, the red block corresponds to a random β particle and the arrow points where the coincidence window closes

There are two ways in which we can correct for this. One, using the rate of beta signals and the time between clock start and the appearance of the prompt peak using the following formula:

$$k_{preemption1} = 1 + (\tau_1 + \delta - D) \times \eta_\beta, \tag{4.9}$$

where τ_1 represents the time between clock start and the appearance of the prompt peak, D is the dead time of the β system, and δ the time interval represented by the single-channel peak at zero, which is an artifact resulting from the way in which the master trigger was established; it contains only random coincidences, their number being proportional to the time width of the β signal used to establish the existence of a coincidence. This method depends on the β rate, which varies from run to run; therefore a weighted averaged of all the runs was used.

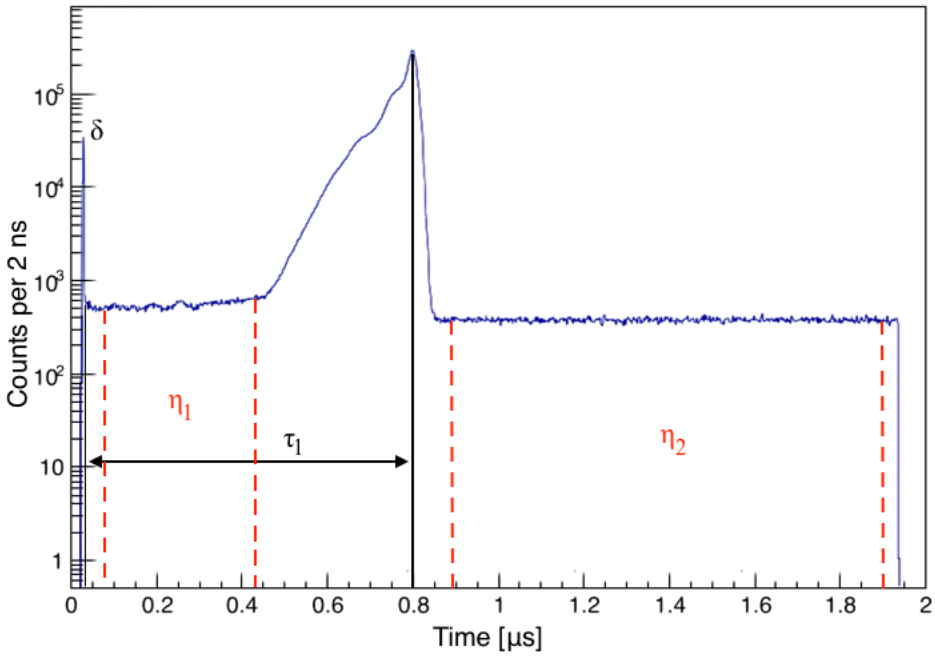

Figure 4.20: TDC spectrum showing the different quantities required for the corrections of the preemption of real coincidences.

For the second, we can calculate the losses using the average rates to the left and right of the prompt peak (η_1 and η_2 in Figure 4.20) and subtracting one from the other; this can be thought of as extending the rate on the right side of the peak towards the left, with the difference being the losses due to preemption (numerator in Eq. 4.10). The correction is thus obtained from the ratio of these losses to the total number of counts in the prompt peak, in the following way:

$$k_{preemption2} = 1 + \frac{(\eta_1 - \eta_2)(\tau_1 + \delta - D)}{N_{peak}}, \tag{4.10}$$

The regions to the left and right of the prompt peak remain flat for the most part, so a wide selection was used to better determine the rates η_1 and η_2. This method does not depend on the run-dependent β rate; however, using the γ-ray areas gives a larger uncertainty. Therefore, the values used for this analysis come from an average of the two, with a systematic

uncertainty arising from the difference between the two methods. These are given in Table 4.3.

		Uncertainty		
Section	$k_{preemption}$	Total	Statistical	Systematic
Low	1.0013	0.0002	0.00006	0.00019
Med	1.0034	0.0003	0.00013	0.00027
High	1.0048	0.0003	0.00017	0.00025

Table 4.3: Preemption correction factors for the total number of β-γ coincidences.

4.4.4 Bremsstrahlung summing

Similar to real-coincidence summing, external bremsstrahlung emitted from the deceleration of positrons in or near the β detector, is another source of coincidence summing. Unlike the previous summing case there is no sum peak produced by the bremsstrahlung radiation that can be analyzed; instead we have a continuous energy spectrum which is indistinguishable from the summed Compton distributions resulting from all detected γ rays. To determine the contribution of the bremsstrahlung to the γ-ray spectrum, the areas of all γ-ray peaks including 511-keV are obtained and multiplied by their corresponding total-to-peak ratios. The summed results are then subtracted from the total number of counts in the γ-ray spectrum with the difference being the contribution from bremsstrahlung. Knowing this contribution and the full-energy-peak efficiency of the HPGe detector for 829-keV γ rays we can then calculate the probability for summing. The resulting loss from the 829-keV peak is 0.2(1)% of the total with the uncertainty coming from the extension of the spectrum below the cutoff region using EGSnrc, similar to what was shown in Figure 4.18.

4.5 Efficiency calculations

It is clear from Eq. 4.5 that in order to determine the superallowed branching ratio we need to rely on the precise absolute efficiency calibration of the HPGe detector and a reasonable understanding of the relative efficiencies of the β detector as well as its dependence on β^+ energy. As stated in section 3.3.1, the absolute efficiency, ϵ_γ, of our detector at 151 mm is known to $\pm 0.2\%$, based on measurements of ten different sources. However, this applies for a highly controlled setting in which the source-to-detector distance can be measures to a fraction of a millimeter. When using the fast tape-transport system this distance varies. Using the laser measurements from our experimental setup, the mean value for the source-to-detector distance is 151.2 mm, so we accounted for this small difference using the CYLTRAN Monte Carlo code [27]. For the 829-keV γ ray, this leads to $\epsilon_\gamma = 2.763(6) \times 10^{-3}$, the value used for Eq. 4.2. The absolute efficiency of the β detector its not required for our measurement but its dependence on energy is of importance. If the detector response function was completely independent from energy the term $\epsilon_\beta/\epsilon_{\beta i}$ would be equal to unity. However, the efficiency does change slightly as a function of the end-point energy. This effect has been studied using different measurements with sources (^{90}Sr, ^{133}Ba, ^{137}Cs, and ^{207}Bi) along with Monte Carlo calculations [26]. This energy dependence is caused by the low-energy electronic threshold which removes a slightly different fraction of the total β spectrum for different end-point energies. This effect is of importance since any change in efficiency from one transition to another affects the intensity of coincident γ rays following that β transition. Using EGSnrc-generated Monte Carlo calculations we can reproduce the experimental β spectrum (see Figure 4.21) making these calculations a reliable source to obtain the efficiency ratios for the transitions of interest. For the case of the 1058-keV transition of interest, $\epsilon_\beta/\epsilon_{\beta i} = 1.0029(10)$.

E_{xi}(keV)	$E_{\gamma i}$(keV)	$\epsilon_{\gamma i}$(%)	$\epsilon_{\beta}/\epsilon_{\beta i}$
228	-	-	0.9985(10)
1058	829.3	0.2763(6)	1.0029(10)
1851	1622.0	0.1729(7)	1.0162(10)
2072	1844.2	0.1569(6)	1.0267(10)
2740	2511.6	0.1214(5)	1.0819(10)

Table 4.4: Detector efficiencies given for particular γ rays, γ_i and β particles emitted in the decay branches β_i, from states E_{xi}.

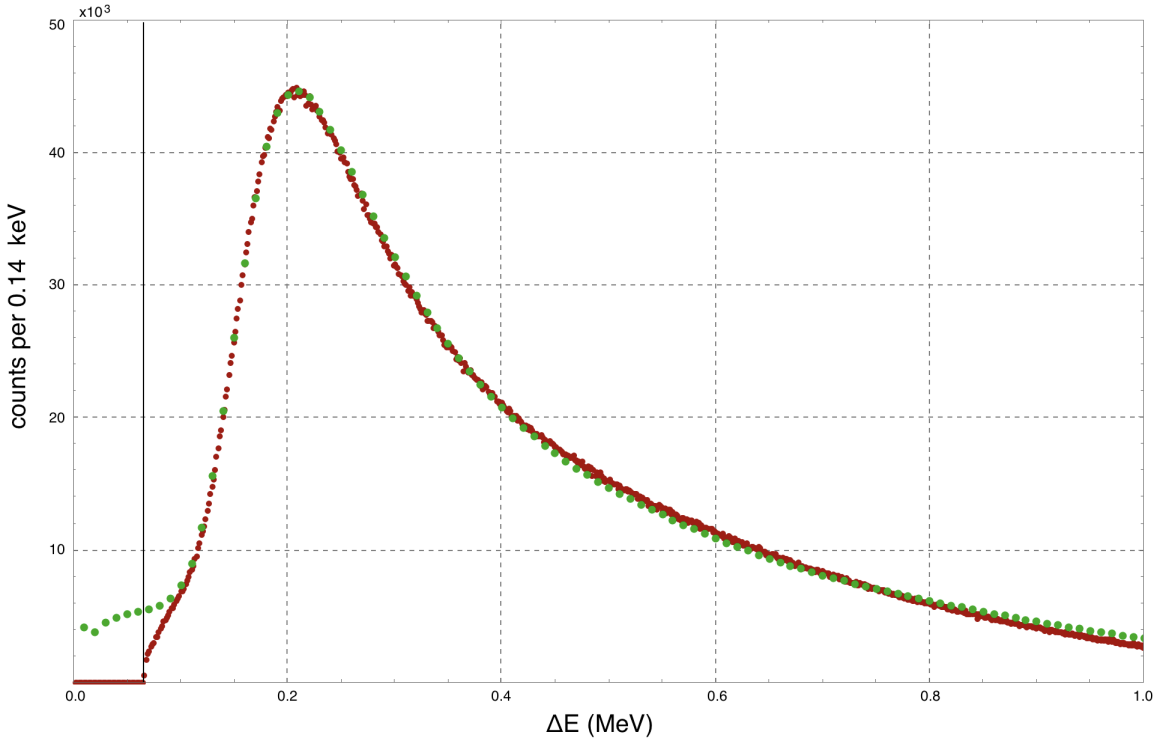

Figure 4.21: The measured energy deposition (red) in the β detector for the decay of ^{26}Si compared to the simulated spectrum (green) obtained from EGSnrc. Solid black line at 60 keV indicates our threshold.

4.6 Corrected $N_{\beta\gamma}$ and N_β

Now that we have obtained all the contributions to the number of β singles and β-γ coincidences we can focus on applying all the corrections so as to extract the values needed for $N_{\beta\gamma}$ and N_β in Eq. 4.5. Starting with N_β:

Section	Total β detector counts ($\times 10^8$)	Background ($\times 10^4$)	^{26}Si fraction	Detected γ rays on β	N_β ($\times 10^8$)
Low	1.07555(10)	-2.924(17)	$\times$0.5691(4)	$\times$0.9988	0.61119(43)
Med	1.99790(14)	-2.341(15)	$\times$0.5691(4)	$\times$0.9988	1.13551(80)
High	2.19880(15)	-1.716(13)	$\times$0.5691(4)	$\times$0.9988	1.24974(88)

Table 4.5: Summary of corrections to the number of β singles.

The total β detector counts in the second column are obtained from the data in each of the β-rate selected regions. The corrections in columns 3-5 were discussed in Sections 4.3.3, 4.3.2, and 4.3.4, respectively, with the background being subtracted while the other two are multiplicative corrections. Once the corrections have been applied (discussed later in this section) the corrected number of β singles are shown in column 6.

In the same manner we can summarize the correction to the number of β-γ coincidences, $N_{\beta\gamma}$. Similar to N_β, the areas for the peaks in column two were obtained from the fitting procedure explained in Section 4.2. The corrections to these areas are shown in columns 3-6, all of them presented in multiplicative form and explained in Sections 4.4.2, 4.4.3, 4.4.1, and 4.4.4 respectively. The corrected areas are then shown in the last column.

Section	829-keV peak Area	Dead time/pileup	Preemption correction	511-keV summing	Bremsstrahlung summing	$N_{\beta\gamma 829}$
Low	34705(238)	×1.0056(70)	×1.0013(2)	×1.0310(14)	×1.0020(10)	36099(258)
Med	63223(279)	×1.0111(39)	×1.0034(3)	×1.0310(14)	×1.0020(10)	66261(404)
High	68719(304)	×1.0160(31)	×1.0048(3)	×1.0310(14)	×1.0020(10)	71471(408)

Table 4.6: Summary of multiplicative corrections to the number of β-γ coincidences.

All corrections, k_i (where i = dead time, summing, preemption, etc.), needed to obtain the total number of β singles and β-γ coincidences have now been evaluated. In order to determine the branching ratio of the transition of interest, we applied all the corrections that have an effect based on the beta rate selection; those corrections include: dead time, preemption of real coincidences, and β background. The use of these corrections can be expressed in the following way:

$$[N'_{\beta\gamma}]_j = [A_{829}]_j \times [k_{deadtime}]_j \times [k_{preemption}]_j, \tag{4.11}$$

$$[N'_{\beta}]_j = [N_{\beta}]_j - [Background]_j, \tag{4.12}$$

where the prime symbol is used to represent a partially corrected quantity and the subscript j represents any of the three β-rate regions: low, med and high. With the rate dependent corrections applied we are able to obtain a ratio between the number of coincidences and the number of β singles, $[N'_{\beta\gamma}/N'_{\beta}]_j$, for all three β rate selected regions. From this, we can determine the weighted average for $[N'_{\beta\gamma}/N'_{\beta}]_j$ and apply the rest of the corrections, all of which have an effect in the same proportion regardless of rate. Applying the rest of the corrections will then result in a fully corrected value of $N_{\beta\gamma}/N_{\beta}$ which can then be use in

Eq. 4.1 to obtain a branching ratio:

$$\frac{N_{\beta\gamma}}{N_\beta} = \left(\frac{N'_{\beta\gamma}}{N'_\beta}\right)_{avg} \times \frac{k_{summing} \times k_{bremsstrahlung}}{k_{SiFraction} \times k_{\beta on\gamma}} \tag{4.13}$$

Putting all these corrected values together with the efficiency of the HPGe detector, $\epsilon_{\gamma i}$ and the β detector efficiency ratio, $\epsilon_\beta/\epsilon_{\beta i}$, for the 829-keV transition of interest from Table 4.4, we get a branching ratio to the 1058-keV state. The branching ratio obtained for this particular state is then,

$$R_{829} = 21.16(12)\%. \tag{4.14}$$

The other weaker transitions still need to be taken into account to obtain the complete Gamow-Teller branch.

4.7 Relative intensities

As discussed previously, in order to obtain the total Gamow-Teller branching ratio we use the intensities of all other γ rays relative to the most intense 829-keV γ ray. To obtain the relative intensities of these γ rays, their areas were also analyzed by the least-squared fitting program GF3, along with the β and γ efficiencies of both detectors for each of the transitions of interest. Table 4.7 includes a list of the relevant γ ray intensities, including a comparison to previous measurements. The agreement is generally satisfactory which is why a weighted average of the three measurements was used as part of the analysis. The values of the weaker γ rays, 1433.7 and 1654.7 keV, were determined using more precise measurements done by Endt et al. [37] for the branchings of secondary states using (p,γ) reactions. The relative intensities take into account feeding from higher states, with weaker γ rays populating and depopulating the states of interest. Figure 4.22 shows a scheme of the energy levels in ^{26}Al populated by ^{26}Si β decay.

	I_γ			
E_γ (keV)	Ref. [38]	Ref. [7]	This work	Average
829.3	1	1	1	1
1433.7	0.0000(96)		0.0015(6)	0.0009(1)
1622.0	0.1245(23)	0.134(5)	0.1322(16)	0.1300(26)
1654.7	0.00145(32)		0.0017(7)	0.0014(1)
1844.2	0.01179(27)	0.016(3)	0.0130(7)	0.0120(4)
2511.6	0.00282(10)		0.0032(5)	0.0028(1)

Table 4.7: Relative intensities of β-delayed γ rays from the β^+ decay of ^{26}Si.

Taking the 1851 keV energy level as an example, there are two γ rays (1622.0 and 1433.7 keV) depopulating the state, meaning that the ratio of the 1851-keV state to the 829-keV state is then 0.1309. Adding up all the transitions for each of the 1^+ exited states of ^{26m}Al this gives us a ratio, $GT_{tot}/GT_{829} = 1.1472(26)$, between the total Gamow-Teller transitions and the most intense branch, which proceeds the 829 keV γ ray . This result combined with the branching ratio to the 1058-keV state from the previous section allows us to determine the total of all Gamow-Teller branches 24.28(15)% after a 0.04% correction for electron capture. Because we measure β-γ coincidences, we see only the effects of positron emission but are blind to the small electron capture effects. This can be calculated as a function of the β end-point energy, $E_{\beta max}$ and Z using the tools available from the National Nuclear Data Center (NNDC) [39].

While higher energy states than those shown in Figure 4.22 could in principle be populated, with their corresponding low intensity γ rays populating other states of interest, no corrections for this were done based on the theoretical calculations done by Brown and Wildenthal [40]. According to these theoretical calculations the probability of these states being populated are of the order of 10^{-5} which are supported by experiment where they have

not been seen.

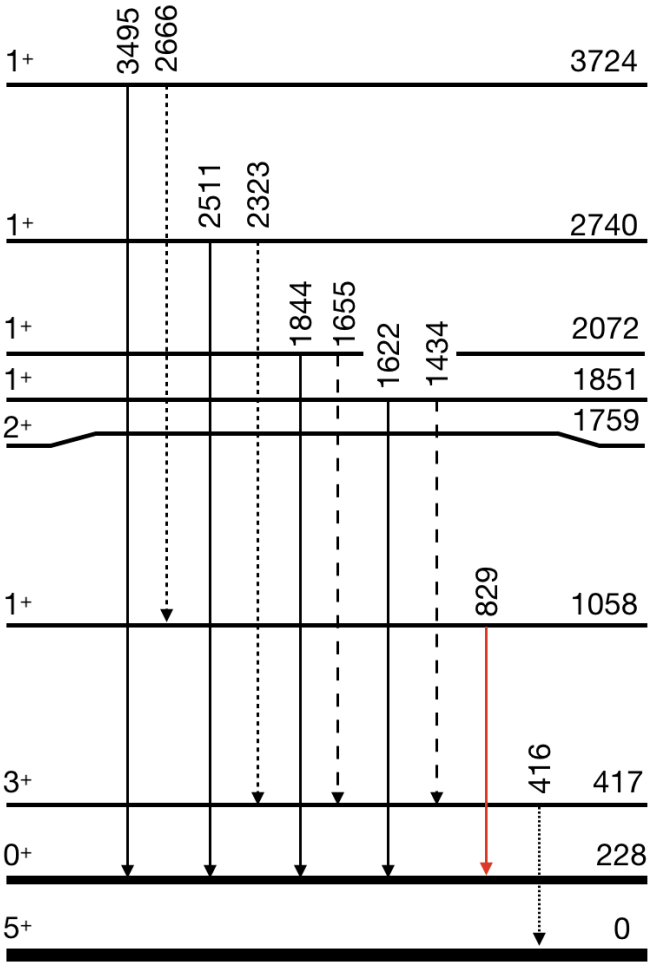

Figure 4.22: Partial level scheme of ^{26}Al, showing the excited states populated by the β decay of ^{26}Si and the γ transitions that occur or may occur following the β decay. The transitions of interest (also shown in Figure 4.1)are represented by solid lines with the most intense highlighted in red. The dashed lines represent weaker observed transitions while the dotted lines identify even weaker transitions that are not observed and for which we can only set an upper limit.

Obtaining the Gamow -Teller branch, allows us to determine the superallowed branch using Eq. 4.1. Leading to,

$$R_F = 1 - 0.2428(15) = 0.7572 \pm 0.0011_{stat.} \pm 0.0004_{syst.}. \tag{5.1}$$

Previous measurements had been done for this branching ratio using the same approach, first by Hardy et al. [7] at Chalk River National Laboratory and later by Matea et al. [41] at the Accelerator Laboratory of the University of Jyvaskyla, the results from both measurements were later incorporated in the most recent survey for superallowed transitions [1] and averaged to a value of 0.7549(57). Our result agrees with the previous ones but significantly reduces the uncertainty by factor of 4. This can be seen in Figure 5.1 below.

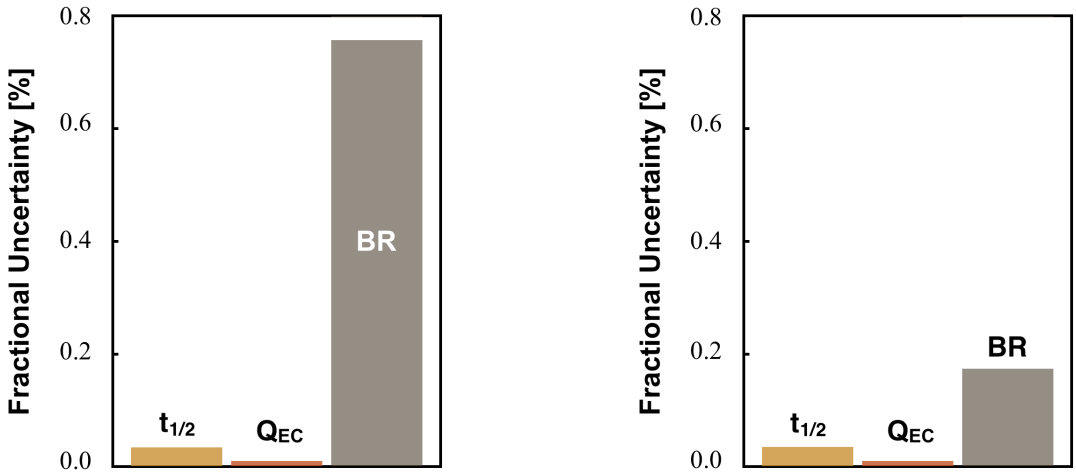

(a) Previous measurements [1]

(b) This work

Figure 5.1: Uncertainty budget comparison.

Now that the branching ratio has been determined, we can use the well-known measurements for the Q_{EC}-value (4840.85(10) keV) [6] and half-life (2245.3(7) ms) [5] to determine the ft value.

The Q_{EC}-value measurements were performed with the JYFLTRAP Penning trap setup at the Department of Physics, University of Jyvaskyla, Finland. The ^{26}Si ions were produced in ^{27}Al(p, 2n)^{26}Si reactions with a 35 MeV proton beam on a 2.0 mg/cm2 aluminum target. The recoiling products were stopped, thermalized and extracted from the IGISOL gas cell through a differentially pumped section into high vacuum and accelerated to 30 keV. After being magnetically separated with a mass resolving power of about 500, the ions having $A/q = 26$ were transported to the JYFLTRAP setup. There the beam was decelerated for injection into the radio frequency quadrupole cooler (RFQ), where the beam was cooled and bunched prior to its transfer to the purification Penning trap [6].

The half-life measurement was done at Texas A&M University using the the same production and experimental set up as the branching ratio measurement discussed in this dissertation (MARS, Fast tape-transport system, etc.) except for a different detections system. A high-efficiency 4π proportional gas counter was employed, instead of the HPGe detector and plastic scintillator, to detect the decay of positrons for 20 half-lives (45 s) with signals from the gas counter being multiscaled into a 500-channel time spectrum. This experiment accumulated data from 5,000 cycles and obtained a half-life with a precision of better than 0.1% [5].

The Q_{EC}-value is needed to determine the statistical rate function, $f(Z, Q_{EC})$. For precision measurements, the integral over the phase space is required to be evaluated at an accuracy of 0.1%. This is accomplished by solving the Dirac equation for the emerging electron moving in the Coulomb field of the nuclear charge distribution [42]. The expression for f is then,

$$f = \xi R(W_0) \int_1^{W_0} pW(W_0 - W)^2 F(Z,W) f_1(W) Q(Z,W) r(Z,W) dW, \qquad (5.2)$$

where W is the electron total energy, W_0 is the maximum value of W ($W_0 = \frac{E_{max}}{m_e c^2} = \frac{Q_\beta}{m_e c^2} + 1$), $p = (W^2 - 1)^{1/2}$ is the electron momentum, Z is the charge number of the daughter nucleus, $F(Z, W)$ is the Fermi function and $f_1(W)$ is the shape-correction function [43], $Q(Z, W)$ is a screening correction [44], and $r(Z, W)$ is an atomic overlap correction. The statistical rate function is calculated using a code developed by Towner and Hardy, the details of which can be found in [2, 45]. The calculation gives us a value of $f = 1028.03(12)$. The half-life and branching ratio are used to determine the partial half-life, $t(t_{1/2}, R)$. The partial half-life is calculated using the following formula:

$$t = \frac{t_{1/2}}{R}(1 + P_{EC}), \tag{5.3}$$

where P_{EC} is the calculated electron-capture fraction, 0.0638%, obtained using the end point energy, $E_{\beta max}$ and the half-life, $t_{1/2}$ as input for the log ft calculator available from NNDC [39]. Using Eq. 5.3 and the values given above, the partial half-life is then $t = 2967.16$ ms with an uncertainty of ± 5.44 ms. The statistical rate function and the partial half-life then give us an ft-value of 3050.3 ± 5.6 s. This result can now be added to the other 14 well-known isotopes and make a contribution to the status of world data.

5.1 Impact on current status of world data

The immediate impact on the current status of world data is the the addition of a new isotope to the set of well-known cases. A new ft value can be added to the set as well as a corrected $\mathcal{F}t$ value (Figure 5.2). The radiative and isospin-symmetry-breaking corrections for ^{26}Si were calculated using the prescribed methods described in Section 2. These values are [1]: $\delta_{R'} = 1.439\%$, $\delta_C = 0.435(27)\%$ and $\delta_{NS} = -0.215(20)\%$. The $\mathcal{F}t$ value shown in

Eq. 2.24 then becomes,

$$\begin{aligned} \mathcal{F}t &= ft(1+\delta'_R)(1+\delta_{NS}-\delta_C) \\ &= ft(1+0.01439)(1-0.00650), \end{aligned} \tag{5.4}$$

where ft takes on the value discussed in the previous section, 3050.3 s, which lead to corrected The $\mathcal{F}t$ value of 3074.1±5.7 s.

The biggest impact on the current status of world data comes from the ft-value ratio of mirror pairs, shown in Eq. 2.33. As discussed earlier, this ratio will help discriminate between the Saxon-Woods and Hartree-Fock radial wavefunctions used in calculating the isospin-symmetry-breaking correction. This result is the second pair of mirror ft-values to be added. The ft-value ratio for the case of $A = 26$ is then,

$$\frac{ft^{^{26}\mathrm{Si}}}{ft^{^{26m}\mathrm{Al}}} = \frac{3050.3(56)}{3037.38(58)} = 1.0043(20). \tag{5.5}$$

Like the A = 38 case, this result favors the Woods-Saxon potential (Figure 5.3) with the $A = 34$ and 42 still to be determined. The two experimental points give a $\chi^2/\nu = 0.60$ for the case of the Wood-Saxons potential, while the Hartree-Fock potential has a $\chi^2/\nu = 4.66$, with $\nu = 1$ degree of freedom. This result certainly favors WS over HF; however it does not completely discard the latter.

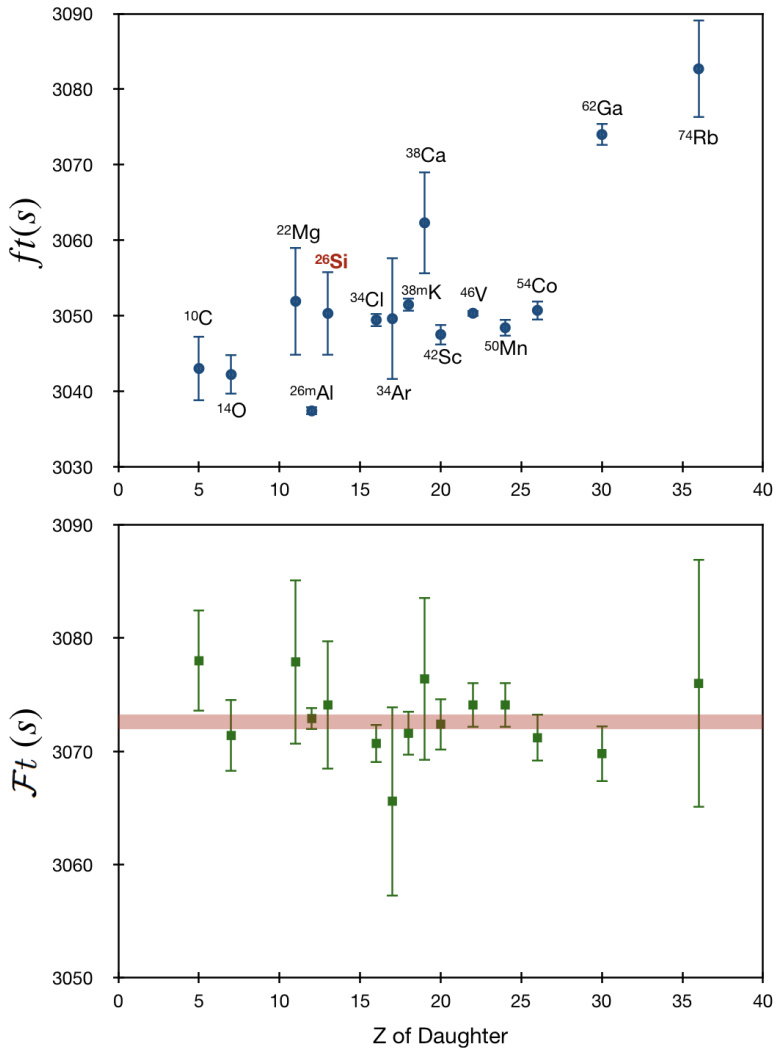

Figure 5.2: (a) Plot of the uncorrected experimental ft values as a function of the charge on the daughter nucleus. (b) The corresponding $\mathcal{F}t$ values are given. The horizontal gray band gives one standard deviation around the average $\mathcal{F}t$ value. The results form ^{26}Si are presented in red.

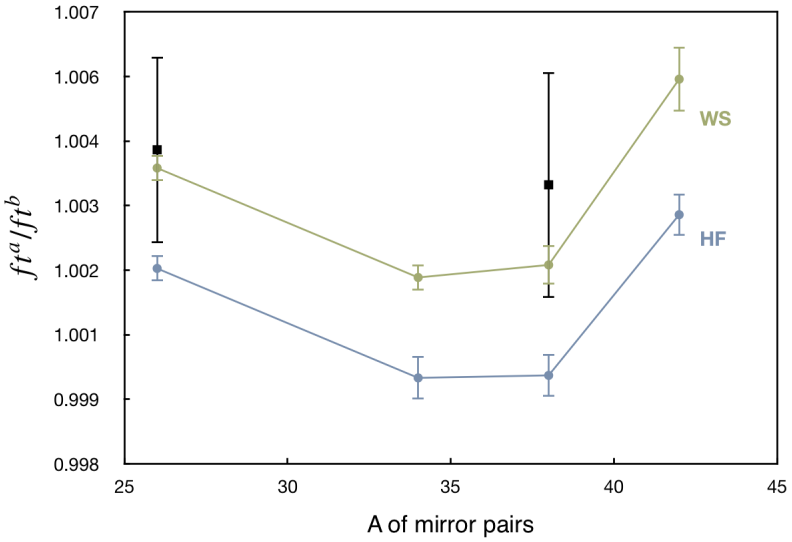

Figure 5.3: Calculated mirror-pair ft^a/ft^b values for $A = 26, 34, 38$, and 42 the four cases currently accessible to high-precision experiment. The green and blue lines connect calculated results that utilize Woods-Saxon (WS) and Hartree-Fock (HF) radial wave functions, respectively. The measured result for the A = 26 and 38 mirror pairs are shown as black squares with error bars.

6. CONCLUSIONS AND FUTURE WORK

We have presented a measurement for the branching ratio of the $T_Z = -1$ superallowed β^+ emitter ^{26}Si. The experimental setup, equipment and analysis procedure for the determination of the superallowed branch have been described in full. Our result for the superallowed branch, 75.72(14)%, was determined by subtracting the total of all other non-superallowed branches, 24.28(14)%, from 100%. This method, used previously for ^{38}Ca [20], allows for a 0.2% precision in the measurement of the superallowed branch to be derived from a 0.6% precision measurement of the non-superallowed branches. This result is now comparable to the precision of the measurements for the half-life, 2245.3(7) ms, and Q_{EC} value, 4840.85(10) keV. With similar precisions for all three quantities we can arrive at an ft value of 3050.3(56) s. Together with the small theoretical corrections, radiative and isospin-symmetry-breaking, we produce an $\mathcal{F}t$ value of 3074.1(57) s. This result agrees with the average $\overline{\mathcal{F}t}$ value of 3072.27(69) s, obtained from 14 different well-know superallowed transitions [1].

Furthermore, this result completes the second pair of superallowed mirror transitions, $^{26}\text{Si} \rightarrow {}^{26m}\text{Al}$ and $^{26m}\text{Al} \rightarrow {}^{26}\text{Mg}$, making it possible to evaluate the ratio of high-precision ft values, which sensitively tests the isospin symmetry-breaking correction required to extract the CKM matrix element V_{ud}. The ratio of ft values, $ft_{^{26}\text{Si}}/ft_{^{26m}\text{Al}}$ is 1.0042(19), using the well-known ft value for ^{26m}Al, 3037.38(58). Similar to the case of the A = 38 pair [4], this experimental result favors the Wood-Saxon radial wavefunctions, bringing us one step closer to solving the systematic uncertainty arising from the choice of potential.

Two more $T_Z = -1$ superallowed emitters, A = 34 and 42, still need to be evaluated to convincingly eliminate one of the potentials used and reduce the uncertainty in V_{ud}. Measurements involving the study of these isotopes are underway and will continue in the immediate future.

REFERENCES

[1] J. C. Hardy and I. S. Towner, Phys. Rev. C **91**, 025501 (2015).

[2] J. C. Hardy and I. S. Towner, Phys. Rev. C **71**, 055501 (2005).

[3] I. S. Towner and J. C. Hardy, Phys. Rev. C **77**, 025501 (2008).

[4] H. I. Park, J. C. Hardy, V. E. Iacob, M. Bencomo, L. Chen, V. Horvat, N. Nica, B. T. Roeder, E. Simmons, R. E. Tribble, and I. S. Towner, Phys. Rev. Lett. **112**, 102502 (2014).

[5] V. E. Iacob, J. C. Hardy, A. Banu, L. Chen, V. V. Golovko, J. Goodwin, V. Horvat, N. Nica, H. I. Park, L. Trache, and R. E. Tribble, Phys. Rev. C **82**, 035502 (2010).

[6] T. Eronen, V. V. Elomaa, U. Hager, J. Hakala, A. Jokinen, A. Kankainen, T. Kessler, I. D. Moore, S. Rahaman, J. Rissanen, C. Weber, and J. Aysto, Phys. Rev. C **79**, 032802 (2009).

[7] J. C. Hardy, H. Scheming, J. S. Geiger, and R. L. Graham, Nucl. Phys. A **246**, 61 (1975).

[8] E. Fermi, Z. Phys. **88**, 161 (1934).

[9] N. Cabibbo, Phys. Rev. Lett. **10**, 531 (1963).

[10] M. Kobayashi and T. Maskawa, Prog. Theor. Phys. **49**, 652 (1973).

[11] E. P. Wigner, Phys. Rev. **56**, 519 (1939).

[12] E. P. Wigner, in *Proceedings of the Robert A. Welch Conferences on Chemical Research*, Vol. 1 (Houston, 1957) p. 67.

[13] J. J. Sakurai, *Modern quantum mechanics* (Addison-Wesley, 1994) p. 239.

[14] R. Feynman and M. Gell-Mann, Phys. Rev. **109**, 193 (1958).

[15] W. J. Marciano and A. Sirlin, Phys. Rev. Lett. **96**, 032002 (2006).

[16] I. S. Towner and J. C. Hardy, Rep. Prog. Phys. **73**, 046301 (2010).

[17] I. S. Towner and J. C. Hardy, Phys. Rev. C **66**, 035501 (2002).

[18] C. Y. Seng, M. Gorshtein, H. H. Patel, and M. J. Ramsey-Musolf, arXiv:1807.10197v1

[hep-ph] (2018).

[19] C. Amsler, M. Doser, M. Antonelli, D. M. Asner, K. S. Babu, *et al.* (Particle Data Group), Phys. Lett. B **667**, 1 (2008).

[20] H. I. Park, J. C. Hardy, V. E. Iacob, M. Bencomo, L. Chen, V. Horvat, N. Nica, B. T. Roeder, E. McCleskey, R. E. Tribble, and I. S. Towner, Phys. Rev. C **92**, 015502 (2015).

[21] R. E. Tribble, R. H. Burch, and C. A. Gagliardi, Nucl. Instr. and Meth. in Phys. Res. A **285**, 441 (1989).

[22] R. E. Tribble, A. Azahari, C. A. Gagliardi, J. C. Hardy, A. Mukhamedzhanov, X. Tang, L. Trache, and S. J. Yenello, Nucl. Phys. A **701** (2002).

[23] Sparrow Corporation, http://www.sparrowcorp.com/ (1997).

[24] V. E. Iacob, R. Burch, J. C. Hardy, P. Lipnik, and L. Trache, Progress in Research 1998-1999, Cyclotron Institue, TAMU.

[25] V. E. Iacob, J. C. Hardy, C. A. Gagliardi, J. Goodwin, N. Nica, H. I. Park, G. Tabacaru, L. Trache, R. E. Tribble, Y. Zhai, and I. S. Towner, Phys. Rev. C **74**, 015501 (2006).

[26] V. V. Golovko, V. E. Iacob, and J. C. Hardy, Nucl. Instr. and Meth. in Phys. Res. A **594**, 266 (2008).

[27] R. G. Helmer, J. C. Hardy, V. E. Iacob, M. Sanchez-Vega, R. G. Nielson, and J. Nelson, Nucl. Instry. Methods Phys. Res., Sect. A **511**, 360 (2003).

[28] R. G. Helmer, N. Nice, J. C. Hardy, and V. E. Iacob, Int. J. Appl. Radiat. Isot. **60**, 173 (2004).

[29] Acuity Laser Measurement, http://www.acuitylaser.com/ (2007).

[30] K. Siegbahn, *Beta- and Gamma-Ray Spectroscopy* (North-Holland Publishing Company, Amsterdam, 1995).

[31] D. C. Radford, Nucl. Instr. and Meth. in Phys. Res. A **361**, 297 (1995).

[32] J. F. Ziegler, http://www.srim.org/ (2008).

[33] Arduino, http://www.arduino.cc/ (2003).

[34] Processing, http://processing.org/ (2001).

[35] P. Finlay *et al.*, Phys. Rev. Lett. **106**, 032501 (2011).

[36] I. Kawrakow, Med. Phys. **27**, 485 (2000).

[37] P. M. Endt, P. De Wit, and C. Alderliesten, Nucl. Phys. **A476**, 333 (1988).

[38] H. S. Wilson, R. W. Kavanagh, and F. M. Mann, Phys. Rev. C **22**, 1696 (1980).

[39] National Nuclear Data Center, www.nndc.bnl.org.

[40] B. A. Brown and B. H. Wildenthal, At. Data Nucl. Data Tables **33**, 347 (1985).

[41] I. Matea, J. Souin, J. Aysto, B. Blank, P. Delahaye, V. V. Elomaa., T. Eronen, J. Giovinazzo, U. Hager, J. Hakala, J. Huikari, A. Jokinen, A. Kankainen, I. D. Moore, J. L. Pedroza, S. Rahaman, J. Rissanen, J. Ronkainen, A. Saastamoinen, T. Sonoda., and C. Weber, Eur. Phys. J. A **37**, 151 (2008).

[42] I. S. Towner and J. C. Hardy, Phys. Rev. C **91**, 015501 (2015).

[43] B. R. Holstein, Rev. Mod. Phys. **48**, 673 (1976).

[44] M. E. Rose, Phys. Rev. **49**, 727 (1936).

[45] J. C. Hardy and I. S. Towner, Phys. Rev. C **79**, 055502 (2009).

[46] P. Oblozinsky and I. Ribansky, Nucl. Instr. and Meth. **73**, 187 (1971).

APPENDIX A

AUTOMATIC DEGRADER CHANGER

The purpose of this project was to design, build and install a remote controlled degrader changer for the fast tape-transport system. The changer allows a more efficient use of beam time by reducing the time it takes for a person to finely adjust the degrader thickness at the beginning of an experimental run. This changer consists of two thin wheels (0.0625 inches thick) with radius 2.50 and 3.85 inches comprising 4 and 8 positions, respectively, for different degrader thicknesses. These wheels can be rotated to different positions by two independent stepper motors using Arduino UNO microcontrollers interfaced with Processing software. The interface was designed to be very straightforward, as it can be seen in Figure A.1.

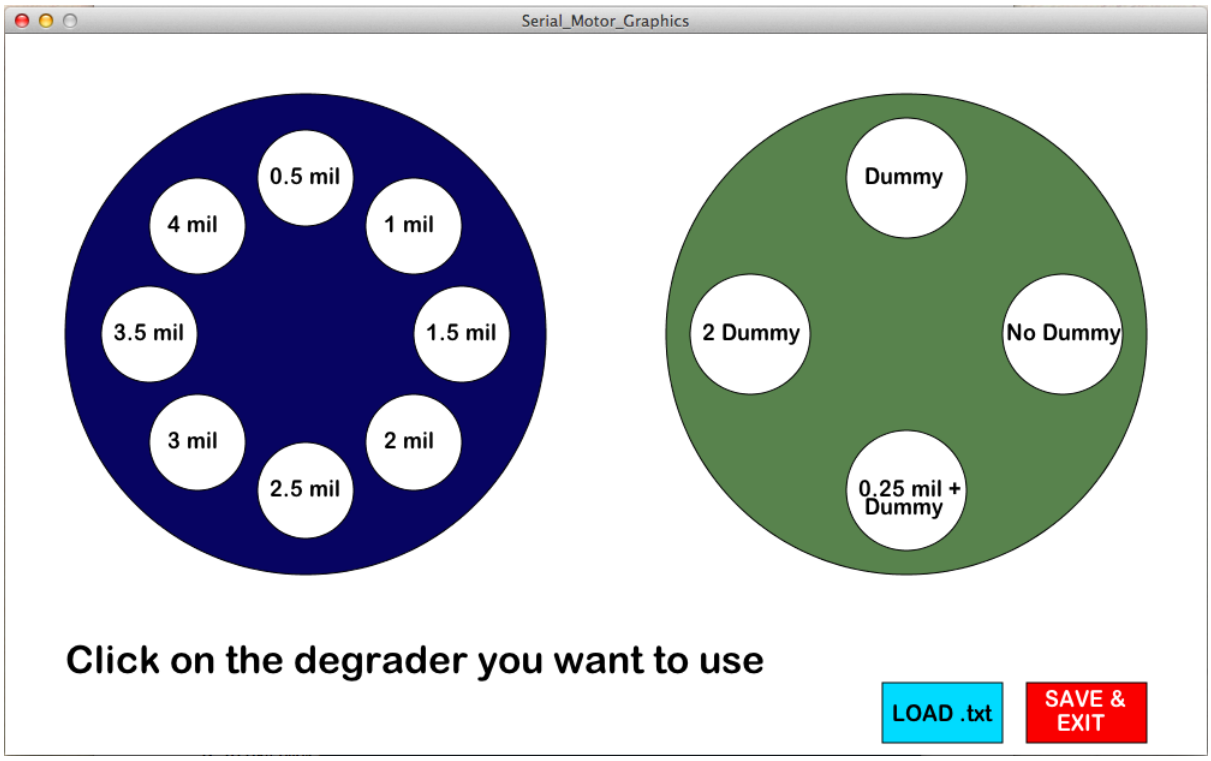

Figure A.1: Graphical user interface for the automatic degrader changer.

Arduino controllers [33] are an open-source based electronics with their own programming language based on Java, C and C++. These microcontrollers provide an efficient way to move the stepping motor to the required position with the precision of a fraction of degree, depending on the number of steps in the motor. Similarly, Processing, an open-source programming language for visual design also based on Java and C, and developed at MIT Media Lab [34], provides the tools to create the interface for the controllers.

Regarding the design, the experimental set up was not to be modified, so this created some spatial restrictions. After creating and reviewing several designs, the wheel design seemed to work best with the restrictions, integrating into the set up as an independent component. Some supports and stands were built to hold the stepper motors in place in order for the degraders to be in the correct position. All components in this project are made out of aluminum for strength and lightness.

Figure A.2 below shows the different parts needed for this project. Everything in grey represents unmodified and essential experimental set up, red shows the supports for the stepper motors (black), green is for a minimally modified degrader stand and blue represents the wheels. Several wheels were made in order to have different sets of Al degraders, these can be changed to satisfy the needs of any experiment. For a case in which more Al is needed, the slightly modified degrader stand is equipped with 4 slots that hold 2 inch Al rings [marked with yellow arrows in Figure A.2 (c)]. Each ring can be set with different degrader thicknesses and placed in a fixed position, allowing the wheel to act as a fine tuning tool. For the particular case of ^{26}Si, a fixed ring with 4.5 mils of aluminum was used while the set of wheels allowed for 0.25 mil additional increments.

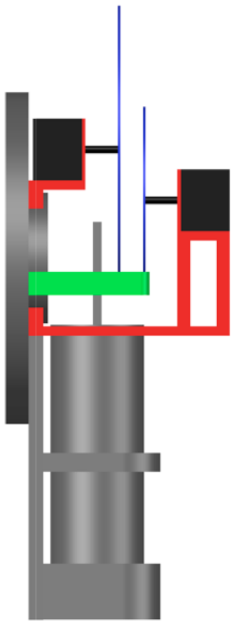

(a) Side view

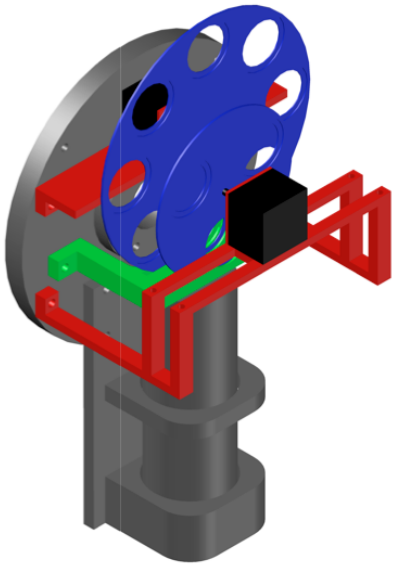

(b) Isometric view

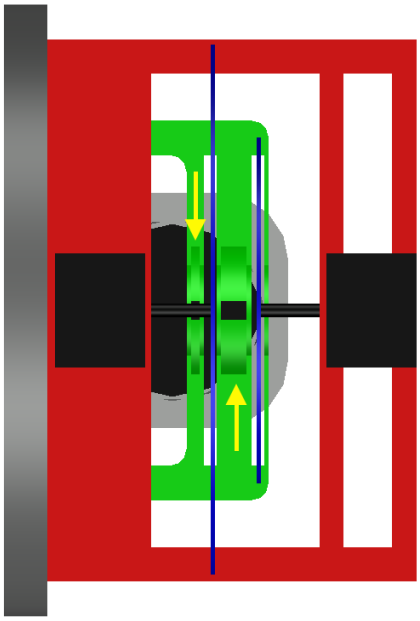

(c) Top view

(d) Picture taken during testing

Figure A.2: Automatic degrader changer CAD.

APPENDIX B

β SCINTILLATOR GEOMETRICAL EFFICIENCY

When the sample is not moved to the appropriate position it affects the efficiency of both the beta and gamma detectors. To illustrate this, a measurement of a ^{90}Sr source deposited on aluminized mylar tape was done in-lab looking at the rate of betas detected as a function of position from the center of the plastic scintillator detector. The source was placed at a distance of 1.5 mm from the Be window and moved transversally in increments of 2 mm. This experiment creates a profile of the efficiency of the plastic scintillator as the source is moved off-center. The dimension of the source is 5 mm in diameter, about 1/2 of the expected diameter of the implanted beam. Figure B.1 shows the schematic for the experimental set up as well as the results obtained.

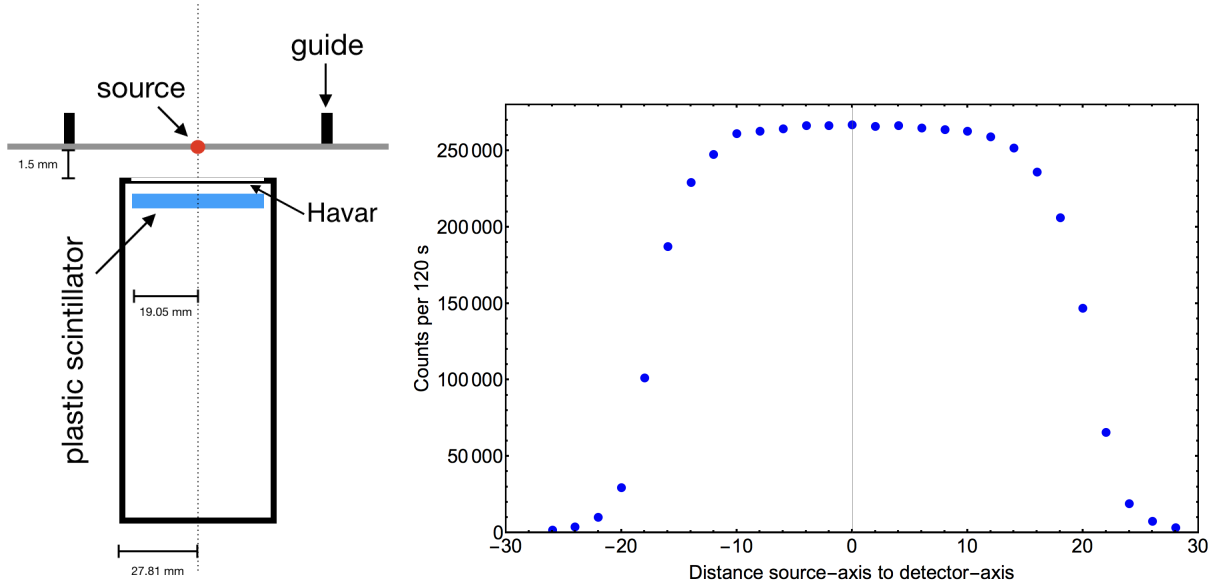

(a) Experimental set up.

(b) ^{90}Sr results.

Figure B.1: Experimental set up and results from ^{90}Sr measurement. It can be seen from the results that around ± 2 cm the efficiency for beta detection already drops by $\sim$50 %.

Each point in Figure B.1(b) was measured for 2 minutes. This time was sufficient to obtain enough statistics for the measurement to be precise to better than 1% precision. After the data were obtained, solid angle calculations for the disk-disk arrangement were used to fit the data so that we could then adjust for the radius of the beam implanted during the on-line experiment. The calculations used were obtained from Oblozinsky and Ribansky [46], the solid angle equation used was,

$$\Omega = 2\pi - \frac{4}{\pi R_s^2}\int_0^{R_s} dqq \int_0^{\pi} d\psi h \int_0^{\pi} d\phi \frac{h^2+\rho^2+R_d\rho\cos\phi}{h^2+\rho^2-\rho^2\cos^2\phi} \times \frac{1}{\sqrt{h^2+\rho^2+R_d^2+2R_d\rho\cos\phi}}, \tag{B.1}$$

with

$$\rho = \sqrt{\rho_0^2 - 2\rho_0 q\cos\psi + q^2}, \tag{B.2}$$

where R_s and R_d are the radii of the source and detector respectively, h the distance source-to-detector and ρ_0 the distance off-axis between the center of the source and detector. This equation assumes the detector lies on the XY-plane and that the Z-axis passes through the center of the source and the X-axis passes through the center of the detector. As can be seen in Figure B.2, the calculations and experiment agree very well with the exception of the edges where the aluminum support of the Havar window starts interfering with the detection of the β particles (see Figure B.1(a)). The small offset in the experimental data compared to Figure B.1(b) come from the way the measurement was made starting with the source on one side of the plastic scintillator and moving the source 2 mm at a time with no precise way of determining a centered source to detector. With the calculation and experiment in agreement we can make the calculations for a source four times the size (20 mm) which resembles the size of the on-line experiment (Figure B.3).

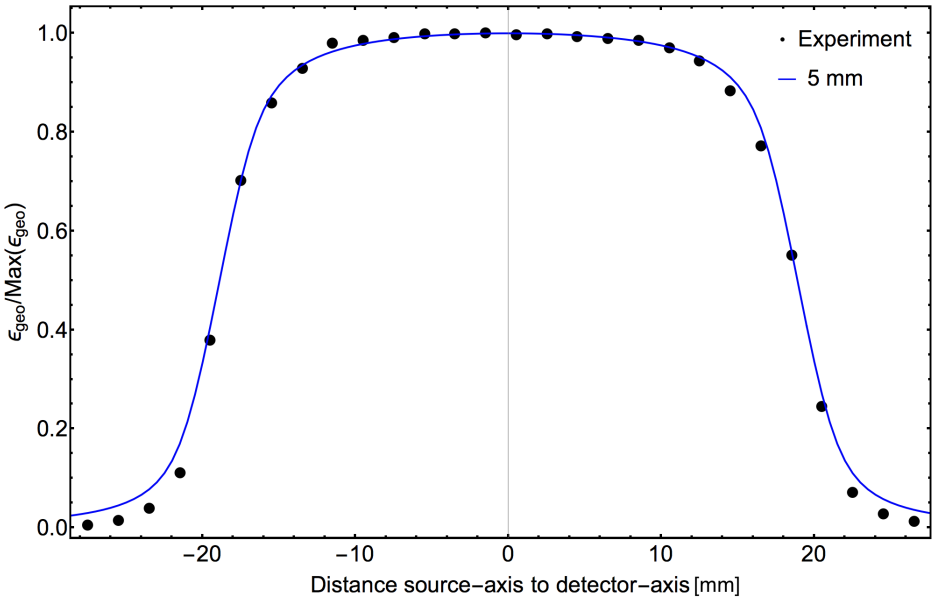

Figure B.2: Geometrical efficiency comparison between calculation and experiment. The points represent the experimental measurement while the solid line represents the results from the numerical evaluation of Eq.B.1.

From our β/HI ratio selection (Figure. 4.3) it can be seen that 90% of the cycles are within a 7% efficiency difference which, from these calculations, translates to a maximum distance of $\pm$9.8 mm from the center position. From the perspective of the β particle detection this not as important as the effect this distance shift might have for the detection of γ rays. Both β singles and β-γ coincidences have the same β efficiency regardless of the position; however, the efficiency of the γ detector might change. If we consider that the γ rays interact approximately 40 mm inside the detector, that means that the distance from the point of interaction to the tape is $151 + 40 = 191$ mm. If we then calculate the average position, assuming the tape has the same probability of stopping at any position between 0 to 9.8 mm, the result is then an added distance of 0.084 mm. The added distance has a 0.09% effect on the HPGe detector efficiency which made our β/HI ratio limits a safe choice for this measurement.

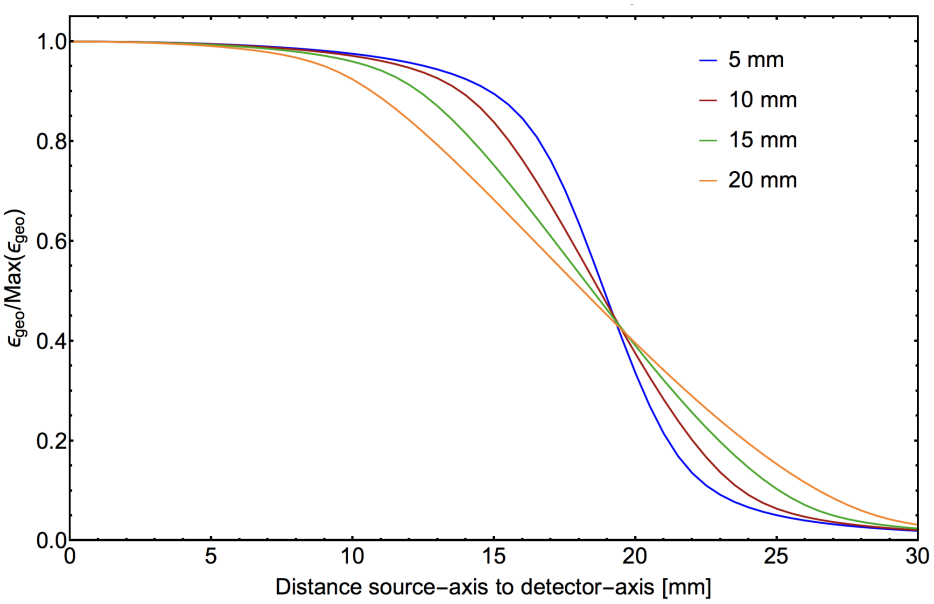

Figure B.3: Geometrical efficiency comparison for sources of different sizes going from 5 mm to 20 mm in diameter. It can be seen that before the 20 mm mark the efficiency drops to $\sim 45\%$.